Role of electronic structure on nitrate reduction to ammonium: a periodic journey

O. Quinn Carvalho,[1] Rylee Marks,[1] Hoan K.K. Nguyen,[1] Molly E. Vitale-Sullivan,[2] Selena C. Martinez,[1] Líney Árnadóttir,[1] Kelsey A. Stoerzinger[1,z]

[1] School of Chemical, Biological and Environmental Engineering, Oregon State University, Corvallis, OR, 97331, USA

[2] School of Mechanical, Industrial, and Manufacturing Engineering, Oregon State University, Corvallis, OR, 97331, USA

[z] Corresponding email: kelsey.stoerzinger@oregonstate.edu

1. Abstract

Electrocatalytic reduction of waste nitrate to ammonium provides a circular process with reduced carbon dioxide emissions compared to current nitrate treatment and ammonia production processes. However, electrocatalysts require a delicate balance between a surfaces' activity for the competing hydrogen evolution (HER) and nitrate reduction reactions (NO_3RR). We measure ammonium Faradaic efficiencies (FEs) of several transition metals (TMs) ranging from 3.6±6.6% (on Ag) to 93.7±0.9% (on Co) in neutral buffered media. A microkinetic model identifies competitive adsorption between nitrate and hydrogen adatoms (H^*) as the origin of voltage-dependent nitrate rate order. NO_3RR FE is described via competition for electrons with the HER, decreasing sharply for TMs with high work function or hydrogen adsorption energy. Density functional theory calculations indicate Co maximizes ammonium selectivity by: (1) binding intermediate nitrite strongly to enable subsequent reduction; and (2) promoting subsequent nitric oxide dissociation, leading to selective reduction of nitrogen adatoms (N^*) to ammonium.

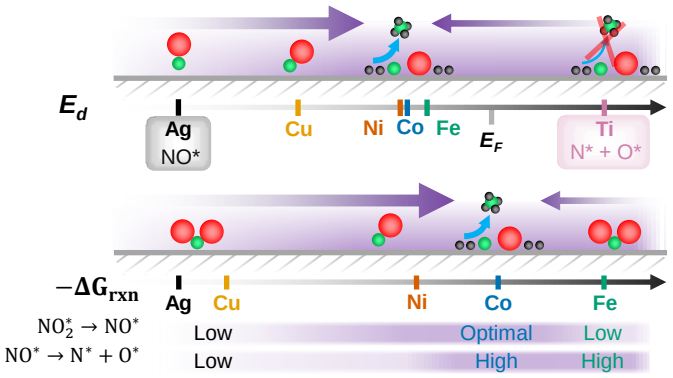

For graphical abstract only

2. Introduction

Nitrate accumulation represents a growing threat to global drinking water resources and human health.[1] At the same time, ammonia production (the largest anthropogenic disruption to

the nitrogen cycle)[2] emits more carbon dioxide than production of any other commodity chemical.[3] Together, this motivates research in technologies that can generate green ammonia, preferably circularly by upgrading waste forms of nitrogen.[4] Electrochemical reduction offers a scalable, distributable, and increasingly economical[5] technology for the upgrading of waste nitrate to value-added products (ammonium[6–8] and hydroxylamine[9]) or benign dinitrogen gas.[10]

Nitrate reduces to ammonium by a complex 8-electron and 10-proton process. In the rate-limiting step, adsorbed nitrate reduces to nitrite.[10] Nitrite is the predominant side product in neutral and alkaline electrolytes,[11–15] reducing further to nitric oxide when remaining adsorbed on the surface (and more complex products when present in the aqueous phase[16]). Nitric oxide serves as a critical intermediate in determining selectivity between nitrogen/oxides and ammonium or hydroxylamine.[17] Mechanistically, adsorbed nitric oxide (NO^*) forms ammonium by one of two pathways: (1) Eley-Rideal like proton-coupled electron transfer (PCET) reducing NO^* to hydroxylamine (NH_2OH^*) and further to ammonium;[18] or (2) dissociation of NO^* into N^* and O^* adatoms and subsequent Langmuir-Hinshelwood like hydrogenation of N^* by H^* to ammonium.[10,19]

Despite these complexities, recent electrochemical NO_3RR literature has demonstrated appreciable FE and selectivity to ammonia in highly alkaline electrolytes. For example, strained Ru nanoparticles—where Ru[20,21] is a benchmark thermal Haber Bosch catalyst—have achieved 100% FE at potentials as cathodic as -0.2 V vs the reversible hydrogen electrode (RHE), albeit at high nitrate concentrations (1 M).[6] First row transition metals such as Co[22,23] and alloys including NiCu[7] have also demonstrated high FE. However, while such examples

exist under alkaline pH, a fundamental understanding of the physicochemical factors driving NO_3RR selectivity towards ammonium is lacking, particularly in the circumneutral pH range expected of most wastewaters.[8,24,25]

Here we investigate electrocatalytic NO_3RR activity and selectivity at low conversion for a series of polycrystalline 3d (Ti, Fe, Co, Ni, $Ni_{0.68}Cu_{0.32}$, and Cu) and $4d^{10}$ (Ag) transition metal foils (TMs) in buffered sodium phosphate electrolyte (pH 7; $Na_xH_{3-x}PO_4$). Trends between phosphate-mediated HER activity and H chemisorption energy[26] correspond with the familiar Sabatier relationship between HER exchange current and metal-H^* bond strength,[27,28] providing an *in-situ* probe of H^* affinity for different TM surfaces. Microkinetic modeling of the competition between the HER and NO_3RR captures experimentally observed potential-dependent nitrate rate order, where peak rate order magnitude and potential are well-described by the difference in H^* and nitrate adsorption free energies ($\Delta G_{H*} - \Delta G_{NO_3^-*}$). The HER and NO_3RR compete for electrons, where HER activity descriptors (TM work function by photoemission[29] and H chemisorption energy[26,28]) play key roles in describing NO_3RR FE. The d-band model[30] provides a fundamental understanding of the relationship between TM electronic structure and nitric oxide adsorption energies, describing to a first order the increased selectivity towards ammonium as the TM d-band center energy (E_d) approaches the Fermi level (E_F). Selectivity can be further explained by the differences in calculated reaction free energies for nitrite reduction $\left(\Delta G_{NO*} - \Delta G_{NO_2^-*}\right)$ and nitric oxide dissociation $(\Delta G_{N*+O*} - \Delta G_{NO*})$, where Co is an optimal catalyst for both of these selectivity-critical reaction steps. Together, the physicochemical parameters of work function, H chemisorption energy, and E_d vs E_F

provide valuable electrocatalyst design parameters for the selective production of green-ammonium from waste nitrate.

3. Results

3.1. Role of H chemisorption energy and HER on NO_3RR activity

We first probe the ability of TM foils to abstract protons from phosphate anions with cyclic voltammetry (CV, Figure 1a and S1). Phosphate-mediated HER (Figure 1a, black dashed lines) is observed as a mass-transfer limited peak at potentials less-cathodic than water-dissociation (Supplementary Figures 1 and 2), where protons are easier to extract from phosphate anions than from water.[31] The comparable mass-transfer limited current density (ca. 2 mA/cm^2_{geo}; Supplementary Figure 1) across TMs indicates similar roughness except for the lower-roughness Ag and Co.

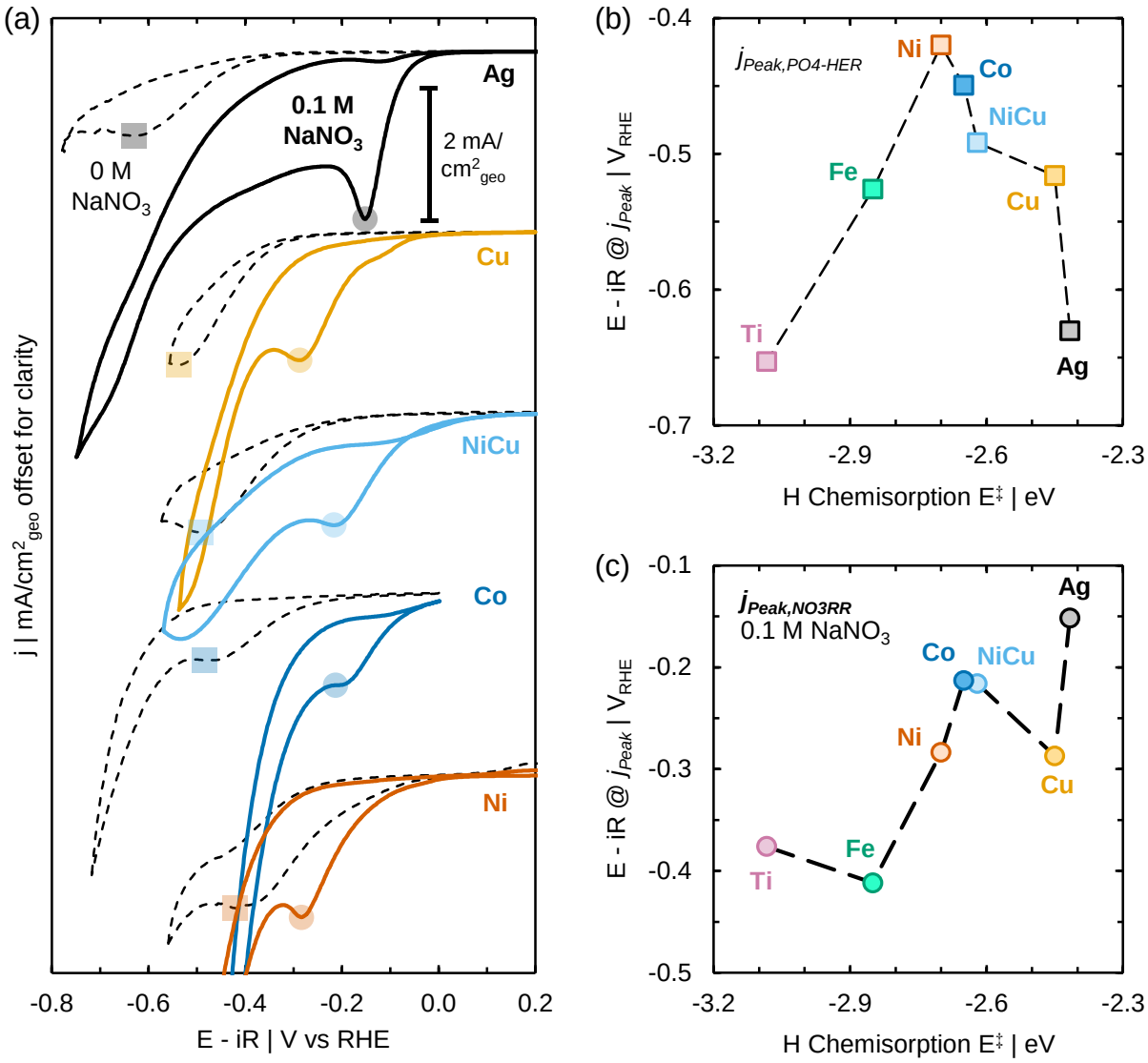

Figure 1. (a) CV collected at 10 mV/s in quiescent 0.1 M $Na_xH_{3-x}PO_4$ in the absence (dashed black trace) and presence (solid colorful trace) of 0.1 M $NaNO_3$ for denoted TM foils. CVs offset for clarity with mass-transfer limited phosphate-mediated HER (squares) and nitrate reduction (circles) denoted. Potential at mass-transfer limited (b) phosphate-mediated HER (E – iR @ $j_{Peak,PO4\text{-}HER}$) and (c) nitrate reduction (E – iR @ $j_{Peak,NO3RR}$) in the presence of 0.1 M $NaNO_3$, both plotted against H chemisorption energy from Ref. [26]. E – iR @ $j_{Peak,NO3RR}$ for Co and Fe are from inflection points (minimum in differential current with respect to voltage) as surrogate for potential at peak current. Data for H chemisorption energy adapted from Ref. [26] and interpolated for $Ni_{0.68}Cu_{0.32}$ (denoted as light blue NiCu) as the sum of molar fractions from Ni and Cu.

The potential at peak phosphate-mediated HER (E – iR @ $j_{Peak,PO4\text{-}HER}$; squares in Figure 1a) exhibits a volcano-style trend with literature H chemisorption energies (Figure 1b), mirroring the well-known relationship between HER exchange current and H chemisorption

energy in acidic electrolytes (Supplementary Figure 3a).[26–28] HER activity on TMs binding H weakly (e.g. Ag, Cu) is limited by proton adsorption, while TMs binding H strongly (e.g. Fe, Ti) are limited by H-H bond formation kinetics.[32] HER activity is also well-described by work function,[29] where higher work function TMs (e.g. Ni and other Group X TMs) demonstrate greater HER activity than those of lower work function TMs (Supplementary Figure 3b).[28]

For CVs in the presence of 0.1 M sodium nitrate (Figure 1a, solid lines), nitrate reduction current becomes apparent at potentials nominally less-cathodic than HER (Supplementary Figures 4 and 5). NO_3RR current manifests as either a shift in the phosphate deprotonation peak to less cathodic potentials (e.g. Ni), or as a second mass-transfer limited peak (e.g. Ag). A Nernstian shift in peak potentials to less-cathodic potentials occurs with increasing logarithmic nitrate concentration (Supplementary Figure 6).

For first-row (3d) TMs, mass-transfer limited nitrate reduction potentials (Figure 1c, E – iR @ $j_{Peak,NO3RR}$) are the least-cathodic for TMs binding H^* slightly weaker than Ni (e.g. Co and $Ni_{0.68}Cu_{0.32}$). Alloying weak H^*-binding Cu with Ni (e.g. $Ni_{0.68}Cu_{0.32}$, denoted NiCu) also shifts NO_3RR onset to less-cathodic potentials than either terminal monometallic composition, consistent with literature in alkaline electrolyte.[7] In contrast, TMs binding H^* strongly (e.g. Fe, Ti) have considerably more-cathodic mass-transfer limited nitrate reduction potentials (Figure 1c and S6), suggesting that strong H chemisorption energy leads to sluggish PCET and hydrogenation kinetics for the NO_3RR.

3.1.1. Microkinetic modeling of potential-dependent nitrate rate order

We next measure nitrate rate order experimentally (Supplementary Figures 7 and 8) and develop a microkinetic model demonstrating the impact of competition between nitrate and H^* on NO_3RR activity (Figure 2). This model describes how thermodynamic and kinetic parameters drive the rate-limiting steps of the HER[33] and NO_3RR. Here we highlight modelling results of three TMs along the weak H chemisorption arm of Figure 1b (*e.g.* Cu, Ni, and $Ni_{0.68}Cu_{0.32}$, see SI for model details and experimental nitrate rate order for additional TMs, Supplementary Figure 8).

For TMs binding H^* weakly (Figure 1b), nitrate rate order exhibits a potential-dependent peak (Figure 2a), reminiscent of a competitive Langmuir-Hinshelwood mechanism.[34] We therefore hypothesize that this peak shape originates from competitive adsorption between H^* and nitrate. Increasing H chemisorption energy corresponds to a decreased peak rate order magnitude and shift to less-cathodic potentials. These experimental rate-order profiles are well-described by our microkinetic model (Figure 2b), assuming reduction of adsorbed nitrate to nitrite is rate limiting (via sequential PCET and/or hydrogenation, Supplementary equations 19-21)[10] and describing HER kinetics (Supplementary equations 7-15) following the work of Shinagawa *et al.*[33] Agreement between experimental (Figure 2a) and modeled (Figure 2b) nitrate rate order versus potential can be achieved by changing only the thermodynamic parameters reflecting the difference in $\Delta G_{H*} - \Delta G_{NO_3^-*}$ ($\propto -\log[K_H/K_{NO_3^-}]$), where $\Delta G_{H*} - \Delta G_{NO_3^-*}$ of Cu is greater (lower relative H^* affinity, Figure 1b) than that of $Ni_{0.68}Cu_{0.32}$ and Ni.

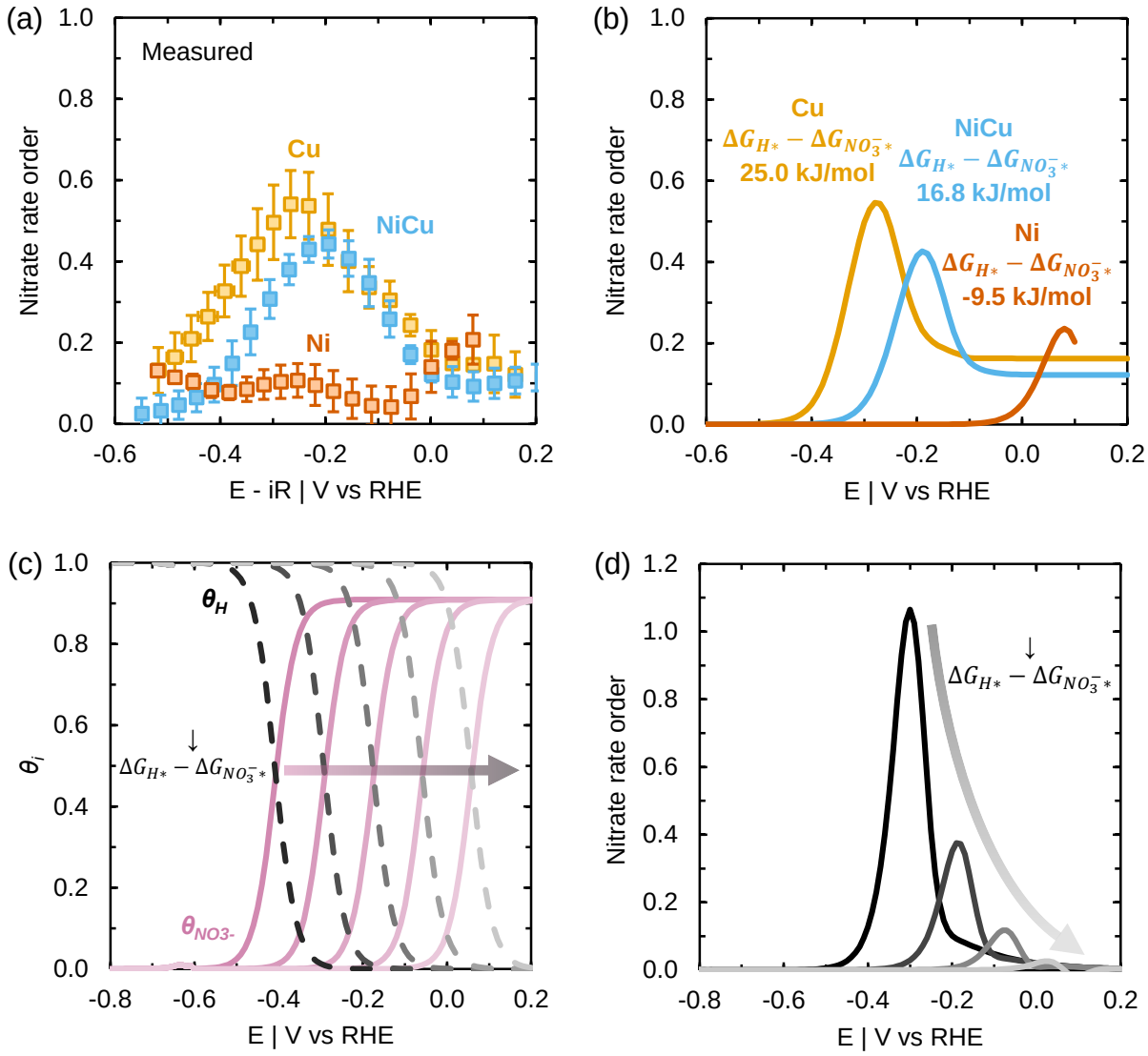

Figure 2. (a) Experimentally measured and (b) microkinetically modelled potential-dependent nitrate rate order, measured by steady-state chronoamperometry in 0.1 M $Na_xH_{3-x}PO_4$ with a series of sodium nitrate concentrations (Supplementary Figure 7) for Cu (golden), $Ni_{0.68}Cu_{0.32}$ (light blue), and Ni (orange). Error bars in (a) denote one standard deviation from the average of at least three (n = 3) separate measurements. Only thermodynamic parameters ($\Delta G_{H*} - \Delta G_{NO_3^-*}$) in (b) are adjusted as denoted to achieve agreement; see Supplementary Table1 for additional model parameters. (c) Potential-dependent fractional H^* (black dashed) and nitrate (fuchsia solid) coverage for a series of H^* to nitrate adsorption coefficients (K_H:K_{NO3}) denoted by increasingly light shades in order of 10^{-7}, 10^{-5}, 10^{-3}, 10^{-1}, and 10^{1}. (d) Nitrate rate order for a series of K_H:K_{NO3} denoted by increasingly light shades of grey in order of 10^{-5}, 10^{-3}, 10^{-1}, and 10^{1}.

The potential at maximum rate order ($E_{max\ rate}$) serves as a direct indicator of $\Delta G_{H*} - \Delta G_{NO_3^-*}$ for TM surfaces (Supplementary Figure 13). Potential-dependent nitrate coverage is

implicitly derived from a competitive adsorption isotherm with H* (Supplementary equations 13 and 18; Figure 2c). At potentials where H* coverage is low (E >> HER), modeled nitrate coverage is defined by the material-dependent nitrate adsorption coefficient ($K_{NO_3^-}$) and the activity of solution-phase nitrate anions ($\alpha_{NO_3^-}$, approximated here as concentration; Supplementary equation 18). H*, having explicitly potential-dependent coverage (Supplementary equation 13), displaces nitrate at increasingly cathodic potentials, where the potential with equivalent H* and nitrate coverage ($\theta_H = \theta_{NO_3^-}$) is proportional to $\Delta G_{H*} - \Delta G_{NO_3^-*}$ (Supplementary Figure 10). Further, $E_{max\ rate}$ coincides with the potential where $\theta_H = \theta_{NO_3^-}$ (Supplementary Figure 10), providing optimal reactant coverages to facilitate Langmuir-Hinshelwood-like nitrate reduction mechanisms (Supplementary equations 20 and 21). As the potential where $\theta_H = \theta_{NO_3^-}$ shifts cathodically with increasing $\Delta G_{H*} - \Delta G_{NO_3^-*}$ (Figure 2c), rate order magnitude increases (Figure 2d) due to the exponential dependence of nitrate reduction on overpotential (Supplementary equations 19-21, Supplementary Figure 13c). This provides a physical interpretation of why $\Delta G_{H*} - \Delta G_{NO_3^-*}$ dictates both $E_{max\ rate}$ and rate order magnitude, while the ratio of kinetic parameters (reaction rate constants; k_{NO3RR}:k_{HER}) only controls magnitude (Supplementary Figure 13b).

3.2. NO_3RR FE and selectivity to ammonium: dependence on bulk electronic structure

We first introduce potential-dependent NO_3RR FE and ammonium selectivity data for Cu and Ni foils (Figure 3), expanding to include the role of alloying in this system (Figure 4) and additional monometallic TMs (Figures 5 and 6). Cu demonstrates appreciable (>70%) NO_3RR

FE at potentials prior to the onset of water-dissociative HER (>-0.6 V vs RHE; Figure 3a). Within this range of potentials, the majority of charge passed to nitrate results in formation of nitrite with a minority fraction designated to ammonium formation (*ca.* 10-20%). However, the onset of water-dissociative HER (CV at top of Figure 3a) increases selectivity towards ammonium at the expense of total NO_3RR FE (≤ -0.6 V vs RHE), suggesting elevated H^* coverage mediates hydrogenation of reduced nitrogenous species ($NO_{x,ads}$).

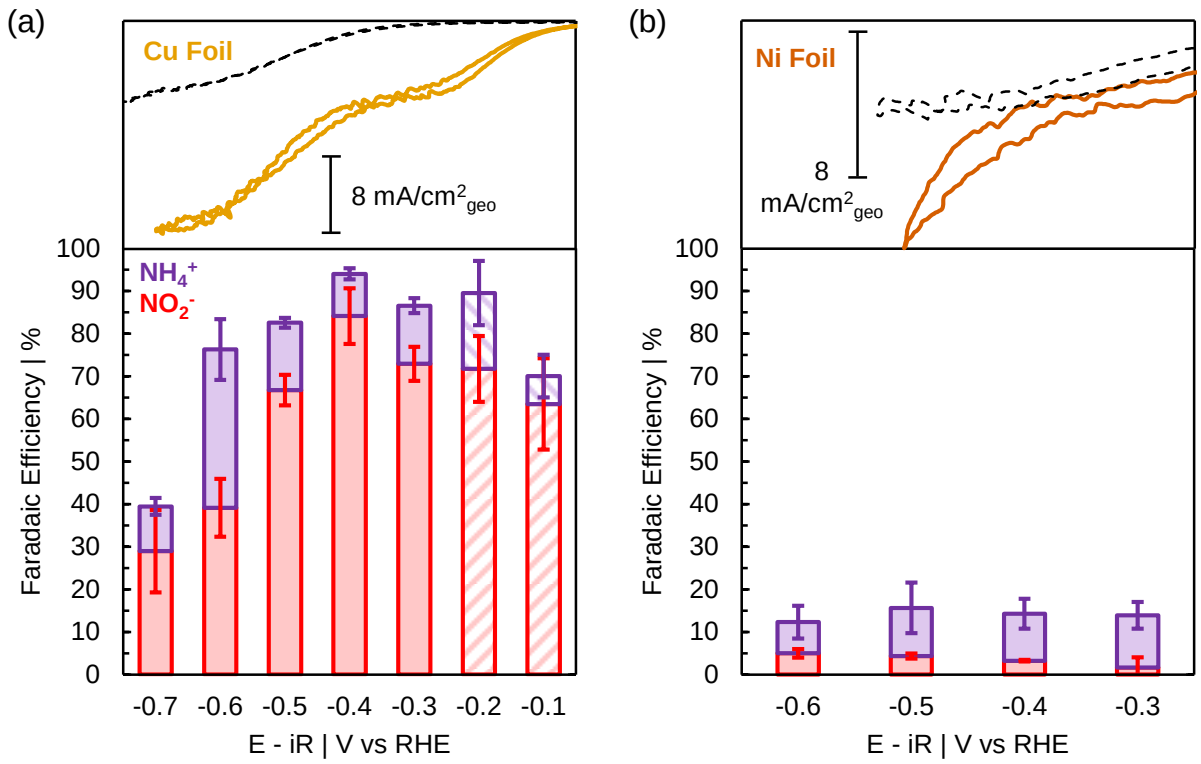

Figure 3. Top: CVs of (a) Cu and (b) Ni collected at 10 mV/s in stirred 0.1 M $Na_xH_{3-x}PO_4$ in the absence (dashed black lines) and presence (solid lines) of 0.1 M $NaNO_3$. Top of panel denotes 0 mA/cm^2_{geo} with 8 mA/cm^2_{geo} scale bar for reference. Bottom: FE to nitrite (red bars) and ammonium (purple bars) for (a) Cu and (b) Ni foils after passing 0.2 (solid) or 0.04 e^-/NO_3^- (hatched) by 85% iR-corrected chronoamperometry in stirred 0.1 M $Na_xH_{3-x}PO_4$ with 0.1 M $NaNO_3$. Error bars denote one standard deviation of the average of at least three (n = 3) separate measurements.

In contrast to Cu, Ni demonstrates poor NO_3RR FE (10-15%) across the range of potentials

measured here (Figure 3b). A qualitative assessment of CVs in stirred electrolyte (top panels of Figure 3) reinforce this observation, where the ratio of current in the presence and absence of nitrate on Ni is much lower than that of Cu. However, electrons contributing to NO_3RR on Ni primarily form ammonium (50-90%). Ammonium selectivity on Ni decreases with increasingly cathodic potentials, unlike all other TMs measured here (Supplementary Figures 16 and 17). This suggests adsorbed H^* are more likely to form dihydrogen than to hydrogenate nitrate as cathodic potential is increased, or that mass-transfer limited phosphate deprotonation (top panel of Figure 3b) hinders the formation of proton-rich ammonium (10 H^+/NH_4^+ from nitrate).

As discussed in the Introduction section, the ammonium-formation mechanism abides by one of two pathways: PCET of associatively-adsorbed NO^* (Ref. [18]) or dissociative adsorption of nitric oxide and subsequent hydrogenation of N^* adatoms by H^*.[10,19] Activation of a Langmuir-Hinshelwood like NO^* hydrogenation pathway (e.g. $NO^* + H^*$) may explain the source of enhanced ammonium selectivity on Cu at HER-relevant potentials. Nitric oxide adorbs associatively on low H^* chemisorption energy Cu (Supplementary Figure 18),[35,36] where ammonium formation by PCET is likely predominant, only activating the Langmuir-Hinshelwood mechanism after appreciable H^* coverage is achieved (e.g. cathodic of HER onset). In contrast, Ni— preferring dissociative[35,36] nitric oxide adsorption—likely only forms ammonium by a Langmuir-Hinshelwood like N^* adatom hydrogenation, where our rate-order analysis and microkinetic modelling indicate high H^* affinity at all potentials measured here.

3.2.1. Tailoring electronic structure towards ammonium selectivity by alloying

Motivated by the high ammonium selectivity of Ni and NO_3RR FE of Cu, we next consider the FE and selectivity of a $Ni_{0.68}Cu_{0.32}$ alloy. In circum-neutral electrolyte, $Ni_{0.68}Cu_{0.32}$ foil demonstrates potential-dependent NO_3RR FE (Figure 4a), and selectivity towards ammonium (b), nominally intermediate of the two terminal compositions (e.g. Cu and Ni). Similar to Cu, $Ni_{0.68}Cu_{032}$ demonstrates appreciable (*ca*. 70-80%) FE at potentials less-cathodic than the onset of HER (>-0.6 V_{RHE}), though has much greater selectivity towards ammonium (*ca*. 40-60%) at comparable potentials. Selectivity towards ammonium increases at the expense of FE with the onset of HER (-0.6 V_{RHE}), similar to observations on Cu of potential-dependent competition between nitrate reduction intermediates and H^* for surface sites and NO_3RR and HER for electrons. Note, the larger error bars of $Ni_{0.68}Cu_{0.32}$ relative to Ni or Cu may result from differences in surface composition resultant from surface preparation (see SI methods).

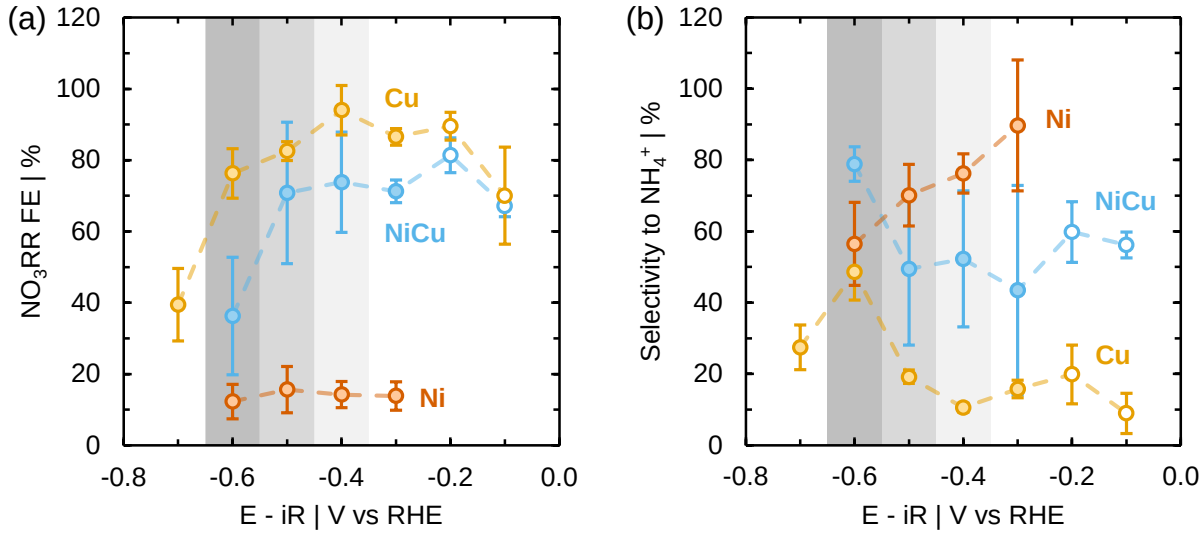

Figure 4. (a) NO_3RR FE and (b) ammonium selectivity for Cu (golden), Ni (orange), and $Ni_{0.68}Cu_{0.32}$ (light blue) measured by 85% iR-corrected chronoamperometry to 0.2 (closed) or 0.04 (open symbols) e^-/NO_3^- in stirred 0.1 M $Na_xH_{3-x}PO_4$ with 0.1 M $NaNO_3$. Shaded bars denote the potential window where HER becomes competitive with NO_3RR, and is used to compare NO_3RR FE and selectivity to ammonium for all TMs in Figures 6 and 7. Error bars denote one standard deviation of the average of at least three (n = 3) separate measurements.

3.2.2. Dependence of intermediate adsorbate energy on TM electronic structure

We propose selectivity towards ammonium is greater on surfaces favoring dissociative nitric oxide adsorption and subsequent N^* adatom hydrogenation by H^* (Figure 3 and 4). Here we discuss the relationship between nitric oxide adsorption and dissociation energies and TM electronic structure by DFT. We limit our discussion to elements in metallic state under the NO_3RR conditions considered here, with consideration of Ti (uncertain surface oxidation state)[37,38] in the SI (Supplementary Table 3).

Our theoretical calculations identify nitric oxide free energy of adsorption (ΔG_{NO*}) becomes more negative as TM E_d approaches E_F (Figure 5a), in-line with descriptions of other simple adsorbates.[30,39,40] Dissociation activation barriers decrease with reaction enthalpy

($\Delta(E_{N*+O*} - E_{NO*})$) and E_d vs E_F (Supplementary Figure 22), in-line with Brønsted-Evans-Polanyi (BEP) scaling relationships.[36,41] This suggests preferential associative adsorption on weak-binding TMs (e.g. Ag and Cu; $\Delta G_{NO*} < \Delta G_{N*+O*}$) and dissociative adsorption on strong-binding TMs (e.g. $Ni_{0.68}Cu_{0.32}$, Ni, Co, and Fe; $\Delta G_{NO*} > \Delta G_{N*+O*}$), in line with prior literature on stepped surfaces (Supplementary Figure 18) and *in vacuo* single crystal adsorption studies.[35,36] Assuming N* can only be hydrogenated to ammonium as a terminal reduction product, this increased preference towards dissociative nitric oxide adsorption could lead to enhanced selectivity towards ammonium on TMs where E_d approaches and overcomes E_F.

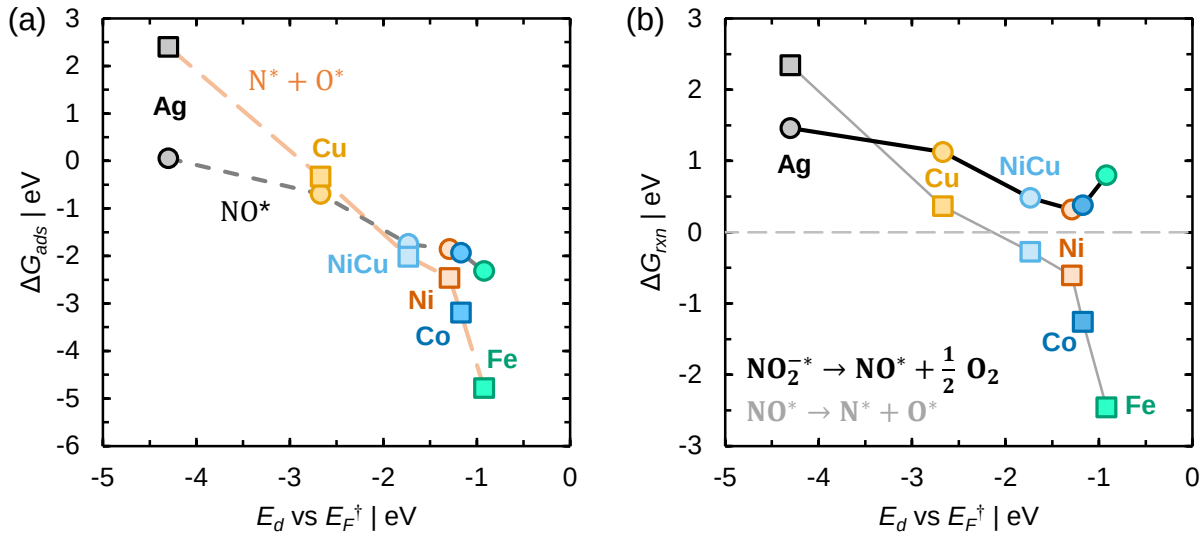

Figure 5. (a) Free energy of associative (circles with short black dashes) and dissociative (squares with long orange dashes) nitric oxide adsorption against E_d vs E_F for denoted TM surfaces. (b) Reaction free energies (ΔG_{rxn}) of nitrite reduction to nitric oxide (circles with thick black lines) and nitric oxide dissociation (squares with thin grey lines) against E_d vs E_F for denoted TMs. Dashed grey line in (b) denotes zero reaction free energy for clarity. The lowest energy surfaces for each crystal structure were used for calculation: fcc(111), bcc(110), or hcp(0001).[42] † Data for E_d vs E_F adapted from Ref. [30].

Understanding the material-dependent driving force for nitrite (the predominant NO_3RR

side-product in neutral and alkaline electrolytes)[11–15] reduction may shed further light on trends in ammonium selectivity. We next compare the calculated free energy difference between nitrite and nitric oxide ($\Delta\left(G_{NO*} - G_{NO_2^-*}\right)$, Figure 5b circles). Deoxygenation is assumed to occur by PCET common across all catalysts and is treated here by including ½ O_2 as a product in the reaction free energy difference; i.e. NO_2^{-*} → NO^* + ½ O_2. The free energy of nitrite adsorption $\left(\Delta G_{NO_2^-*}\right)$ scales with both that of associative (ΔG_{NO*}) and dissociative (ΔG_{N*+O*}) nitric oxide adsorption (Supplementary Figure 23), in-line with scaling relationship for molecules of similar functionality.[43] As E_d approaches E_F, $\Delta\left(G_{NO*} - G_{NO_2^-*}\right)$ becomes increasingly negative up to Ni, then increases for Co and Fe. Assuming the BEP relationship holds for electrochemical reduction of nitrite to nitric oxide,[44] a more negative $\Delta\left(G_{NO*} - G_{NO_2^-*}\right)$ would then correspond to a lower activation barrier, increasing the preference towards nitrite reduction to nitric oxide (and possibly further to ammonium) over desorption.

3.2.3. Role of electronic structure on selectivity towards ammonium

Informed by results from the Ni-Cu system (Figure 4) and theoretical calculations (Figure 5), we expand our study to consider the role of TM electronic structure (work function[29] and E_d vs E_F[30]) and H^* affinity (H chemisorption energy[26]) on NO_3RR FE and selectivity to ammonium. We focus our discussion on potentials with nominal competition between HER and NO_3RR (-0.4, -0.5, and -0.6 V_{RHE}; Figures 6 and 7), with data for additional potentials provided as Supplementary Figures 16 and 17 and Supplementary Table 2.

Considering NO_3RR FE and ammonium selectivity graphically provides a simple means to identify promising electrocatalysts (Figure 6), which appear increasingly towards the upper-right. TMs such as Cu and Ag, while demonstrating appreciable NO_3RR FE, provide poor selectivity to ammonium. At increasingly cathodic potentials, selectivity towards ammonium does increase for these TMs, though at the cost of NO_3RR FE (Supplementary Figures 16 and 17). Alternatively, TMs such as Ni and Ti demonstrate the opposite behavior: providing high selectivity towards ammonium with low NO_3RR FE. Optimally, Fe and (in particular) Co demonstrate both appreciable NO_3RR FE and selectivity towards ammonium.

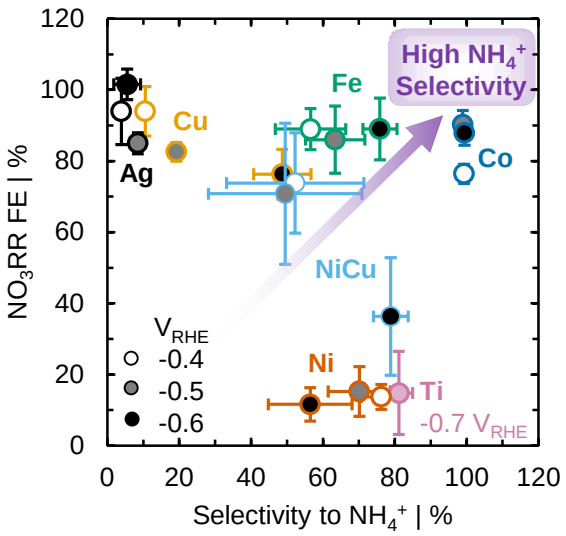

Figure 6. NO_3RR FE against selectivity to ammonium for a series of TM foils, measured in stirred 0.1 M $Na_xH_{3-x}PO_4$ with 0.1 M $NaNO_3$ by 85% iR-corrected chronoamperometry to 0.2 e^-/NO_3^- at -0.4, -0.5, and -0.6 V_{RHE} (denoted).

As NO_3RR FE represents electron selectivity between HER and nitrate reduction, it is best described via H^* affinity towards TM surfaces and the associated electronic descriptor of work function (Figure 7a and Supplementary Figure 20). NO_3RR FE is appreciable (>70%) for TMs

with a broad range of work function and low-to-intermediate H chemisorption energy (e.g. Ag, Cu, Co, Fe), but drops for TMs with either high work function (e.g. Ni, Figure 7a) or high H chemisorption energy (e.g. Ti, Supplementary Figure 20). Ni (and $Ni_{0.68}Cu_{0.32}$) has the greatest work function, and consequently greatest HER activity (Supplementary Figure 3),[28] of the TMs investigated here, demonstrating poor NO_3RR FE due to facile H-H coupling kinetics. In contrast, low work function Ti has the strongest H chemisorption energy, providing H^*-saturated surfaces that impede nitrate adsorption and/or hydrogen bond formation kinetics (i.e. PCET or hydrogenation).[26,28,38] The dependence of nitrate rate order on $\Delta G_{H*} - \Delta G_{NO_3^-*}$ discussed in Section 3.1.1 may provide additional context for understanding the relationship between NO_3RR FE and work function as a future direction for the field. Differences in NO_3RR FE are expected to be more pronounced for lower nitrate concentrations typical of e.g. groundwater (~1.5 mM).[6,7,11,23,45]

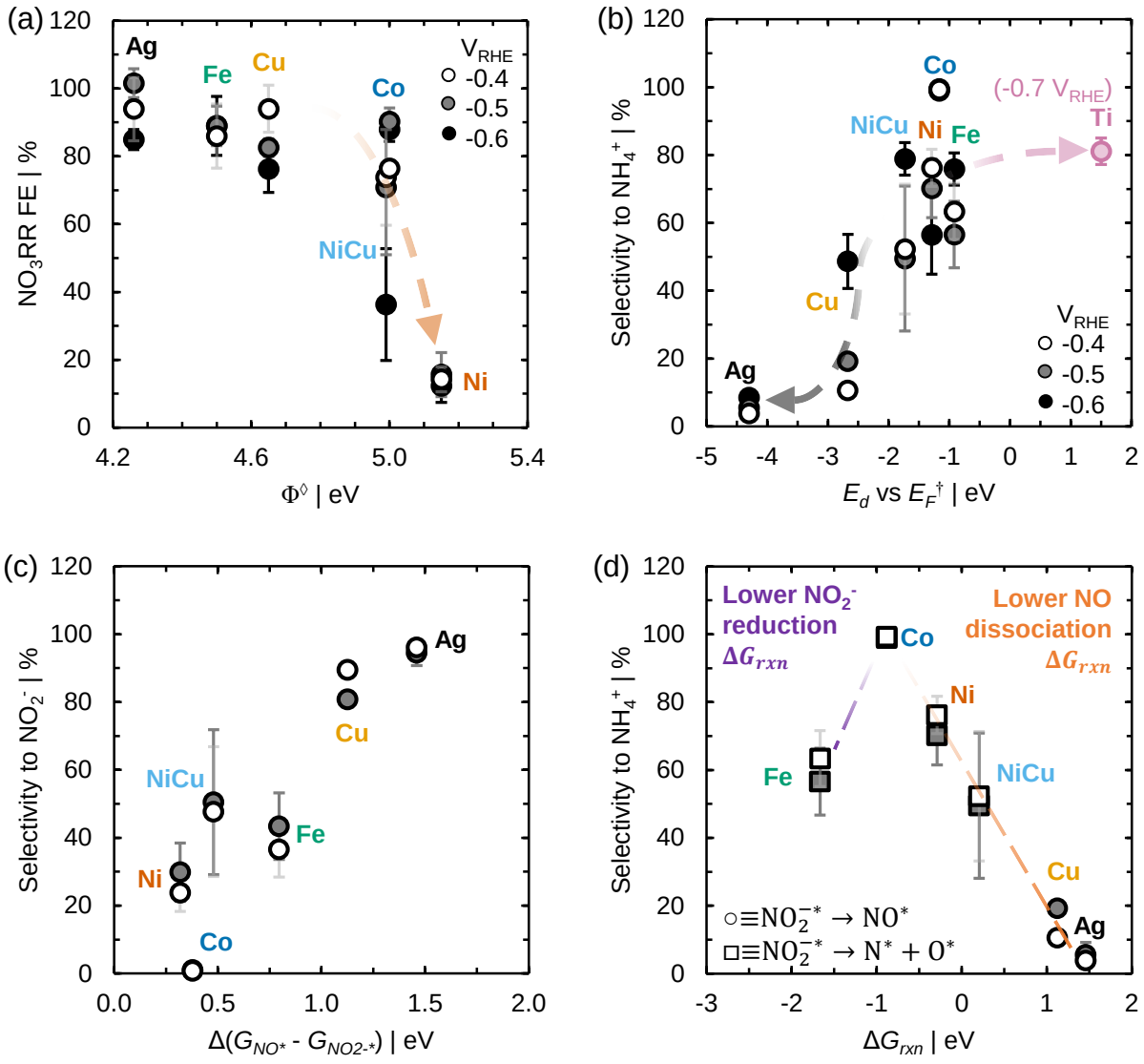

Figure 7. (a) NO_3RR FE against work function and (b) selectivity towards ammonium against E_d vs E_F for denoted TM foils measured by 85% iR-corrected chronoamperometry to 0.2 e^-/NO_3^- at select potentials (-0.4, -0.5, and -0.6 V_{RHE}; denoted), except for Ti where -0.7 V_{RHE} is used to obtain sufficient current. Lines to guide the eye. Ti is excluded from (a) due to uncertainties in work function[29,46] and surface termination (e.g. oxidation state or presence of hydrides),[37,38] but is included in Supplementary Figure 20 for reference. (c) Selectivity to nitrite at -0.4 and -0.5 V_{RHE} against calculated reaction free energy for nitrite reduction to nitric oxide. (d) Selectivity to ammonium at -0.4 and -0.5 V_{RHE} against calculated reaction free energies of nitrite to nitric oxide (circles) and dissociated N^* and O^* adatoms (squares), with lines to guide the eye. Error bars denote one standard deviation of the average of at least three (n = 3) separate measurements. Potential-dependent average and standard deviation of selectivity to ammonium for Co overlaps within the size of the symbols used (see Supplementary Table 2). $^{\Diamond\,\dagger}$ Data for work function adapted from Ref. [29] and E_d vs E_F from Ref. [30], with values (a,b) for $Ni_{0.68}Cu_{0.32}$ interpolated from literature values for Ni and Cu.

We next consider the role of TM E_d vs E_F on selectivity towards ammonium (Figure 7b).

For TMs with E_d well below E_F (e.g. Cu, Ag) selectivity towards ammonium is very low (typically <20%), though increases with H^* coverage under more cathodic applied potentials (Supplementary Figures 16 and 17). In contrast, selectivity towards ammonium is nominally high for E_d approaching E_F (e.g. Ni, Co, Fe), remaining high for TMs with E_d well above E_F (e.g. Ti). This observation can be explained by the d-band model:[30,47,48] the antibonding molecular orbital formed between adsorbed nitric oxide and the TM surface becomes increasingly unoccupied as E_d approaches and overcomes E_F , manifesting as stronger binding (more negative ΔG_{NO*}) and a preference towards dissociative adsorption ($\Delta G_{N*+O*} < G_{NO*}$, Figure 5). Increased ammonium selectivity for TMs that favor NO dissociation leads us to propose that N^* selectively forms ammonium at the potentials considered here. While the d-band model includes an adsorption energy penalty proportional to the overlap integral squared (V_{ad}^2), we find tabulated values of V_{ad}^2 do not describe well the trends in either NO_3RR FE (Supplementary Figure 20) or selectivity towards ammonium (Supplementary Figure 21), suggesting E_d vs E_F predominates this description.

While the d-band model provides a first approximation for understanding trends in ammonium selectivity, the ammonium selectivity of Co is exceptionally high (>95%) across the range of potentials measured here (-0.2 to -0.7 V_{RHE}; Supplementary Figures 16 and 17) compared to materials of similar E_d vs E_F. To better understand the exceptional ammonium selectivity of Co we consider the calculated reaction free energies of nitrite reduction to nitric oxide and its further dissociation (Figure 7c,d). Selectivity to nitrite nominally decreases as $\Delta\left(G_{NO*} - G_{NO_2^-*}\right)$ decreases (Figure 7c). However, while nitrite reduction is more favorable

on Ni than Co, Ni demonstrates a poorer ammonium selectivity than Co. In this case, Ni has a much lower driving force for nitric oxide dissociation than Co (Figure 5b), where we hypothesize N^* selectively reduces to ammonium at the potentials considered here. In contrast, while nitric oxide dissociation is more favorable on Fe compared to Co, nitrite reduction on Fe is less favorable (Figure 5b), resulting in greater nitrite selectivity. This explanation produces a Sabatier-like trend where ammonium selectivity is determined by the free energy of nitrite reduction to either nitric oxide or dissociated N^* (Figure 7d): materials with insufficient driving force for either nitric oxide dissociation (e.g. Ag, Cu, $Ni_{0.68}Cu_{0.32}$, Ni; Figure 5b) or nitrite reduction (e.g. Fe) provide sub-optimal ammonium selectivity. Thus, Co represents an optimum where nitric oxide is bound strong enough to prefer dissociation while still maintaining an appreciable driving force for nitrite reduction.

Coupled with our broader understanding of design principles across the range of TMs considered here, these findings suggest that the work function, H chemisorption energy, and E_d vs E_F of Co may serve as optimal catalyst activity and ammonium selectivity design targets. Development of materials spanning the phase space around Co (e.g. $Ni_{1-x}Fe_x$, $Co_{1-x}Fe_x$ or $Co_{1-x}Ni_x$ alloys) may provide a more discrete understanding of this local optimum electronic structure while shifting towards catalysts with greater earth abundance.[49] Further, the onset potential of NO_3RR on Co could be enhanced by alloying with other highly-active TMs (e.g. $Co_{1-x}Cu_x$ alloys),[7] pairing with metal oxides with greater nitrate affinities,[11] or tailoring cation composition and strength within the electrolyte.[50]

4. Conclusions

We have investigated the NO_3RR on a series of polycrystalline TM foils in neutral, buffered (0.1 M $Na_xH_{3-x}PO_4$) electrolyte, identifying physicochemical parameters that govern both activity and selectivity towards ammonium. Motivated by periodic trends in H^* affinities and NO_3RR mass-transfer limited potentials, we derived a microkinetic model describing rate-limiting nitrate reduction to nitrite by a combination of hydrogenation and PCET. Potential-dependent nitrate rate order manifests from a competitive adsorption between H^* and nitrate, and is well described in our microkinetic model by the material-dependent $\Delta G_{H*} - \Delta G_{NO_3^-*}$.

NO_3RR FE originates from competition with HER and is thus well described by HER activity descriptors: high work function TMs demonstrate appreciable HER activity at the detriment of NO_3RR FE, while FE is limited on TMs binding H^* strongly. DFT calculations demonstrate an increasing preference for nitric oxide binding and subsequent dissociation as E_d approaches E_F, commensurate with increasing ammonium selectivity, reaching a maximum for Co. However, selectivity decreases for Fe, attributed to reduced driving force for nitrite reduction to nitric oxide. These results identify competing design considerations – linking electronic structure to mechanistic selectivity-limiting steps – offering strategies to improve existing catalysts and design new alloy compositions for NO_3RR to ammonium.

5. Methods

We quantify the formation of nitrite and ammonium, the two primary products at the pH and low conversions measured here,[11–15] over a series of commercial polycrystalline TM foils

at a range of potentials as detailed in the Supplemental Information (SI). To better control nitrate conversion as a variable, a fixed charge is passed per nitrate anion (0.2 or 0.04 e^-/NO_3^-), corresponding to maximum 10 or 2% conversion of nitrate assuming 100% FE towards nitrite. Additional methodologies for activity, selectivity, and density functional theory (DFT) calculations are provided in the SI.

6. Acknowledgments

KAS acknowledges support from Oregon State University as a Callahan Faculty Scholar. RM acknowledges funding from the Pete and Rosalie Johnson Internship Program. OQC acknowledges funding the U.S. DOE SCGSR program, administered by the Oak Ridge Institute for Science and Education for the DOE under contract number DE-SC0014664. Part of this research was performed via Tahoma allocation on a project award 51428 from the Environmental Molecular Sciences Laboratory, a DOE Office of Science User Facility sponsored by the Biological and Environmental Research program under Contract No. DE-AC05-76RL01830.

7. References

1. Maura, A., Haowei, W. & Upmanu, L. National trends in drinking water quality violations. *Proc. Natl. Acad. Sci.* **115**, 2078–2083 (2018).
2. Battye, W., Aneja, V. P. & Schlesinger, W. H. Is nitrogen the next carbon? *Earth's Futur.* **5**, 894–904 (2017).
3. Ammonia: zero-carbon fertiliser, fuel and energy storage. *R. Soc.* 1–40 (2020).
4. Comer, B. M. *et al.* Prospects and Challenges for Solar Fertilizers. *Joule* **3**, 1578–1605 (2019).
5. Werth, C. J., Yan, C. & Troutman, J. P. Factors Impeding Replacement of Ion Exchange with (Electro)Catalytic Treatment for Nitrate Removal from Drinking Water. *ACS ES&T Eng.* **1**, 6–20 (2021).
6. Li, J. *et al.* Efficient Ammonia Electrosynthesis from Nitrate on Strained Ruthenium Nanoclusters. *J. Am. Chem. Soc.* **142**, 7036–7046 (2020).
7. Wang, Y. *et al.* Enhanced Nitrate-to-Ammonia Activity on Copper–Nickel Alloys via Tuning of Intermediate Adsorption. *J. Am. Chem. Soc.* **142**, 5702–5708 (2020).
8. van Langevelde, P. H., Katsounaros, I. & Koper, M. T. M. Electrocatalytic Nitrate Reduction for Sustainable Ammonia Production. *Joule* **5**, 290–294 (2021).
9. Dima, G. E., Rosca, V. & Koper, M. T. M. Role of germanium in promoting the electrocatalytic reduction of nitrate on platinum: An FTIR and DEMS study. *J. Electroanal. Chem.* **599**, 167–176 (2007).
10. Wang, Z., Richards, D. & Singh, N. Recent discoveries in the reaction mechanism of heterogeneous electrocatalytic nitrate reduction. *Catal. Sci. Technol.* **11**, 705–725 (2021).
11. Carvalho, O. Q. *et al.* Role of oxide support in electrocatalytic nitrate reduction on Cu. *Electrochem. Sci. Adv.* Under Review (2022).
12. Pérez-Gallent, E., Figueiredo, M. C., Katsounaros, I. & Koper, M. T. M. Electrocatalytic reduction of Nitrate on Copper single crystals in acidic and alkaline solutions. *Electrochim. Acta* **227**, 77–84 (2017).
13. Liu, H. *et al.* Electrocatalytic Nitrate Reduction on Oxide-Derived Silver with Tunable Selectivity to Nitrite and Ammonia. *ACS Catal.* **11**, 8431–8442 (2021).
14. Bouzek, K., Paidar, M., Sadílková, A. & Bergmann, H. Electrochemical reduction of nitrate in weakly alkaline solutions. *J. Appl. Electrochem.* **31**, 1185–1193 (2001).
15. Fox, C. M. & Breslin, C. B. Electrochemical formation of silver nanoparticles and their applications in the reduction and detection of nitrates at neutral pH. *J. Appl. Electrochem.* **50**, 125–138 (2020).
16. Duca, M., van der Klugt, B. & Koper, M. T. M. Electrocatalytic reduction of nitrite on transition and coinage metals. *Electrochim. Acta* **68**, 32–43 (2012).
17. de Vooys, A. C. A., Koper, M. T. M., van Santen, R. A. & van Veen, J. A. R. Mechanistic Study on the Electrocatalytic Reduction of Nitric Oxide on Transition-Metal Electrodes. *J. Catal.* **202**, 387–394 (2001).
18. Kuwabata, S., Uezumi, S., Tanaka, K. & Tanaka, T. Assimilatory and dissimilatory reduction of nitrate and nitrite with a tris(tetrabutylammonium) nonakis(benzenethiolato)octasulfidohexaferratedimolybdate(3-) modified glassy-carbon electrode in water. *Inorg. Chem.* **25**, 3018–3022 (1986).
19. Ko, B. H., Hasa, B., Shin, H., Zhao, Y. & Jiao, F. Electrochemical Reduction of Gaseous Nitrogen Oxides on Transition Metals at Ambient Conditions. *J. Am. Chem. Soc.* **144**, 1258–1266 (2022).
20. Foster, S. L. *et al.* Catalysts for nitrogen reduction to ammonia. *Nat. Catal.* **1**, 490–500 (2018).
21. Dahl, S., Logadottir, A., Jacobsen, C. J. H. & Nørskov, J. K. Electronic factors in catalysis: the volcano curve and the effect of promotion in catalytic ammonia synthesis. *Appl. Catal. A Gen.* **222**, 19–29 (2001).

22. Deng, X., Yang, Y., Wang, L., Fu, X.-Z. & Luo, J.-L. Metallic Co Nanoarray Catalyzes Selective NH_3 Production from Electrochemical Nitrate Reduction at Current Densities Exceeding 2 A cm^{-2}. *Adv. Sci.* **8**, 2004523 (2021).
23. Kani, N. C. *et al.* Solar-driven electrochemical synthesis of ammonia using nitrate with 11% solar-to-fuel efficiency at ambient conditions. *Energy Environ. Sci.* **14**, 6349–6359 (2021).
24. Katsounaros, I., Dortsiou, M. & Kyriacou, G. Electrochemical reduction of nitrate and nitrite in simulated liquid nuclear wastes. *J. Hazard. Mater.* **171**, 323–327 (2009).
25. Nguyen, T. T. P., Do, B. K. D., Bui, N. N., Pham, M. A. & Nguyen, T. V. Selectiveness of Copper and Polypyrrole Modified Copper Electrodes for Nitrate Electroreduction: A Comparative Study and Application in Ground Water. *ECS Trans.* **53**, 41–52 (2013).
26. Nordlander, P., Holloway, S. & Nørskov, J. K. Hydrogen adsorption on metal surfaces. *Surf. Sci.* **136**, 59–81 (1984).
27. Nørskov, J. K. *et al.* Trends in the Exchange Current for Hydrogen Evolution. *J. Electrochem. Soc.* **152**, J23 (2005).
28. Trasatti, S. Work function, electronegativity, and electrochemical behaviour of metals: III. Electrolytic hydrogen evolution in acid solutions. *J. Electroanal. Chem. Interfacial Electrochem.* **39**, 163–184 (1972).
29. Michaelson, H. B. The work function of the elements and its periodicity. *J. Appl. Phys.* **48**, 4729–4733 (1977).
30. Hammer, B. & Nørskov, J. K. Theoretical surface science and catalysis—calculations and concepts. *Adv. Catal.* **45**, 71–129 (2000).
31. Monteiro, M. C. O., Liu, X., Hagedoorn, B. J. L., Snabilié, D. D. & Koper, M. T. M. Interfacial pH Measurements Using a Rotating Ring-Disc Electrode with a Voltammetric pH Sensor. *ChemElectroChem* **9**, e202101223 (2022).
32. Krishtalik, L. I. Hydrogen Overvoltage and Adsorption Phenomena. Part III. Effect of the Adsorption Energy of Hydrogen on Overvoltage and the Mechanisms of the Cathodic Process. in *Advances in electrochemistry and electrochemical engineering, Volume 7* (eds. Delahay, P. & Tobias, C. W.) (Interscience Publishers, 1970).
33. Shinagawa, T., Garcia-Esparza, A. T. & Takanabe, K. Insight on Tafel slopes from a microkinetic analysis of aqueous electrocatalysis for energy conversion. *Sci. Rep.* **5**, 13801 (2015).
34. Singh, N. *et al.* Aqueous phase catalytic and electrocatalytic hydrogenation of phenol and benzaldehyde over platinum group metals. *J. Catal.* (2020) doi:10.1016/j.jcat.2019.12.034.
35. Brown, W. A. & King, D. A. NO Chemisorption and Reactions on Metal Surfaces: A New Perspective. *J. Phys. Chem. B* **104**, 2578–2595 (2000).
36. Bligaard, T. *et al.* The Brønsted–Evans–Polanyi relation and the volcano curve in heterogeneous catalysis. *J. Catal.* **224**, 206–217 (2004).
37. Thomas, N. T. & Nobe, K. Kinetics of the Hydrogen Evolution Reaction on Titanium. *J. Electrochem. Soc.* **117**, 622 (1970).
38. Liu, M. J. *et al.* Catalytic Performance and Near-Surface X-ray Characterization of Titanium Hydride Electrodes for the Electrochemical Nitrate Reduction Reaction. *J. Am. Chem. Soc.* **144**, 5739–5744 (2022).
39. Hammer, B. Special Sites at Noble and Late Transition Metal Catalysts. *Top. Catal.* **37**, 3–16 (2006).
40. Liu, J.-X., Richards, D., Singh, N. & Goldsmith, B. R. Activity and Selectivity Trends in Electrocatalytic Nitrate Reduction on Transition Metals. *ACS Catal.* **9**, 7052–7064 (2019).

41. Logadottir, A. *et al.* The Brønsted–Evans–Polanyi Relation and the Volcano Plot for Ammonia Synthesis over Transition Metal Catalysts. *J. Catal.* **197**, 229–231 (2001).
42. Patra, A., Jana, S., Constantin, L. A., Chiodo, L. & Samal, P. Improved transition metal surface energies from a generalized gradient approximation developed for quasi two-dimensional systems. *J. Chem. Phys.* **152**, 151101 (2020).
43. Abild-Pedersen, F. *et al.* Scaling Properties of Adsorption Energies for Hydrogen-Containing Molecules on Transition-Metal Surfaces. *Phys. Rev. Lett.* **99**, 16105 (2007).
44. Akhade, S. A., Nidzyn, R. M., Rostamikia, G. & Janik, M. J. Using Brønsted-Evans-Polanyi relations to predict electrode potential-dependent activation energies. *Catal. Today* **312**, 82–91 (2018).
45. Pennino, M. J., Compton, J. E. & Leibowitz, S. G. Trends in Drinking Water Nitrate Violations Across the United States. *Environ. Sci. Technol.* **51**, 13450–13460 (2017).
46. Fukuda, Y., Elam, W. T. & Park, R. L. Absolute 2p3/2 core binding energies and work functions of 3d transition-metal surfaces. *Phys. Rev. B* **16**, 3322–3329 (1977).
47. Shiotari, A., Koshida, H. & Okuyama, H. Adsorption and valence electronic states of nitric oxide on metal surfaces. *Surf. Sci. Rep.* **76**, 100500 (2020).
48. Spivey, T. D. & Holewinski, A. Selective Interactions between Free-Atom-like d-States in Single-Atom Alloy Catalysts and Near-Frontier Molecular Orbitals. *J. Am. Chem. Soc.* **143**, 11897–11902 (2021).
49. Vesborg, P. C. K. & Jaramillo, T. F. Addressing the terawatt challenge: scalability in the supply of chemical elements for renewable energy. *RSC Adv.* **2**, 7933–7947 (2012).
50. Katsounaros, I. & Kyriacou, G. Influence of the concentration and the nature of the supporting electrolyte on the electrochemical reduction of nitrate on tin cathode. *Electrochim. Acta* **52**, 6412–6420 (2007).

Supplemental Information:
Role of electronic structure on nitrate reduction to ammonium: a periodic journey

O. Quinn Carvalho,[1] Rylee Marks,[1] Hoan K.K. Nguyen,[1] Molly E. Vitale-Sullivan,[2] Selena C. Martinez,[1] Líney Árnadóttir,[1] Kelsey A. Stoerzinger[1,z]

[1] School of Chemical, Biological and Environmental Engineering, Oregon State University, Corvallis, OR, 97331, USA

[2] School of Mechanical, Industrial, and Manufacturing Engineering, Oregon State University, Corvallis, OR, 97331, USA

[z] Corresponding email: kelsey.stoerzinger@oregonstate.edu

1. Experimental

1.1. Electrocatalytic characterization

Activity for a series of TM foil working electrodes was evaluated in a cylindrical glass three-electrode cell by CV and steady-state current density measured by chronoamperometry (steady-state CA), with a Pt coil counter electrode and Ag/AgCl (CH Instruments CHI111; saturated KCl) reference electrode calibrated daily to the reversible hydrogen electrode (RHE). Prior to activity and selectivity measurements, TM foils were cleaned by etching in a 1:4 ratio of hydrochloric acid to water for 30 seconds, followed by rinsing in water and drying under dinitrogen flow. While this etching step is intended to provide a reproducible surface composition for monometallic TM foils, it may induce compositional variability in the $Ni_{0.68}Cu_{0.32}$ alloy used in this study (see note in Figure 4).

CV was performed at 10 mV/s in quiescent and 500-rpm stirred $Na_xH_{3-x}PO_4$ (dibasic sodium phosphate monohydrate (Na_2HPO_4 x H_2O), Fischer Chemical, Certified ACS Grade; monobasic sodium phosphate (NaH_2PO_4), Fischer Chemical, Certified ACS Grade) aqueous solution with a series of sodium nitrate ($NaNO_3$; EMD Millipore, ACS Grade) concentrations, with reported data representing a reproducible trace. Steady-state CA measurements were performed for 30 s per potential in 40 mV increments with a stir bar rotating at 500 rpm to mitigate mass transfer limitations. The voltage range for each TM foil was chosen to observe phosphate-deprotonation and water-dissociation mediated hydrogen evolution (HER), limiting the anodic potential to exclude the formation of surface oxides (excluding Ti which forms surface oxides or hydrides[1] across the potential range considered here).[2] Potentials of CV and

CA measurements have been corrected for solution and contact resistance (iR) losses by identifying the real impedance contribution from potentio electrochemical impedance spectroscopy (PEIS).[3–5] Current has been normalized by the geometric surface area (cm^2_{geo}) as measured by ImageJ software.

1.2. Selectivity

Selectivity measurements were performed in a Pine Research low volume separated H-cell, with *ca.* 20 mL of 0.1 M $Na_xH_{3-x}PO_4$ in both the anode and cathode compartment, separated by a Nafion 117 (Fuel Cell Store) cation-exchange membrane. The cathode compartment, containing the working electrode and Ag/AgCl reference housed in an Ametek K0065 secondary frit, was sparged with Ar for 30 minutes prior to introducing 0.1 M $NaNO_3$ by addition of 3 M $NaNO_3$ with 0.1 M $Na_xH_{3-x}PO_4$. After a further 15 minutes of Ar sparging, an initial aqueous-phase sample (0.3 mL) was withdrawn prior to applying a bias to the working electrode. The range of potentials measured for each TM includes only those achieving appreciable current density (*ca.* <-0.1 mA/cm^2_{geo}) to limit individual measurements to at most six hours to circumvent appreciable electrolyte evaporation. A final aqueous-phase sample (0.3 mL) was withdrawn after passing a pre-determined amount of charge passed with respect to added nitrate concentration (0.2 or 0.04 e^-/NO_3^-). The anode compartment contained a graphitic carbon rod (Becker Brothers) counter electrode. Potentials were 85% iR corrected by EC-Lab software during CA selectivity measurements with solution and contact resistances typically *ca.* 5-20 Ω. Thermal catalysis, the environment (e.g. Ar-sparging), and the Nafion membrane

used to separate anode and cathode compartment provide negligible sources of ammonium and nitrite when measured at longer time scales than those considered here.[6]

FE of species i (FE_i) was calculated as,

$$FE_i(Q) = \frac{(c_i(Q) - c_i(0))n_i F}{Q/V} \times 100\% \quad [1]$$

where $c_i(Q)$ is the concentration of species i at a charge (Q) corresponding to a given e^-/NO_3^-, n_i denotes the number of electrons needed to convert one molecule of nitrate to one molecule of species i $(n_{NO_2^-} = 2\ e^-; n_{NH_4^+} = 8\ e^-)$, F is Faraday's constant (96,485 C/mol e^-), and Q/V is the number of e^-/NO_3^- normalized by the volume of electrolyte in the cathode compartment of the H cell. Selectivity (S_i) was calculated as,

$$S_i(Q) = \frac{FE_i(Q)}{FE_{NO_2^-}(Q) + FE_{NH_4^+}(Q)} \times 100\% \quad [2]$$

where it is assumed that nitrite (NO_2^-) and ammonium (NH_4^+) are the primary products. Standard deviation from the average of n measurements was determined from the sample standard deviation (s) equation

$$s = \sqrt{\frac{\sum_{i=1}^{n}(x_i - \bar{x})^2}{n-1}} \quad [3]$$

where x_i is the i^{th} measurement and $\bar{x}$ is the average of all n measurements.

1.3. Analytical techniques for determining selectivity

Of the 0.3 mL sample aliquots, 15 µL was diluted to 1.5 mL with water for detection of nitrate and nitrite by ion chromatography (IC; Thermo Scientific Dionex ICS-5000). The IC was operated with a Dionex IonPac CG16 5 x 50 mm guard column, eluent flowrate of 0.7 mL/min 15 mM sodium hydroxide (NaOH; Thermo-Fisher), 40 °C column temperature, and

25 μL sample volume. Standard curve and elution time were determined from a series of sodium nitrite ($NaNO_2$), sodium nitrate ($NaNO_3$; EMD Millipore, ACS Grade), and sodium phosphate buffer ($Na_xH_{3-x}PO_4$; mixture of mono- (NaH_2PO_4; Fischer Chemical, Certified ACS Grade) and di-basic (Na_2HPO_4 x H_2O; Fischer Chemical, Certified ACS Grade) sodium phosphate required to achieve pH 7) aqueous solutions. A spectrophotometric plate reader (BioTek Synergy 2) was used to detect ammonium at 660 nm wavelength by a modified Berthelot reaction, as described elsewhere.[7] Briefly, triplicate 50 μL volumes were loaded into a 300 μL 96-well plate with a series of ammonium nitrate (NH_4NO_3; Fischer Chemical, Certified ACS) concentrations in 0.1 M $Na_xH_{3-x}PO_4$ for standard curve development. Berthelot reagents included trisodium citrate (Beantown Chemical, 99.0%), 2-phenylphenol sodium salt (Fischer Chemical, 99%), sodium nitroprusside dihydrate (MP Biomedicals, ≥ 99%), trisodium phosphate (Fischer Scientific, ≥ 96.0%), trisodium citrate (Macron Fine Chemicals, ACS Reagent Grade), and sodium hypochlorite (Clorox, 7.4%).

1.4. Density functional theory

Periodic density functional theory (DFT) calculations were carried out with Vienna Ab-initio Simulation Package (VASP).[8–10] The Kohn-Sham equations are solved self-consistently with electron exchange and correlation described by Perdew, Burke, and Ernzerhof functional (PBE)[11] with the Projector Augmented Wave (PAW)[12,13] method.

The calculated (experimental) bulk lattice constants for fcc Ag, fcc Cu, fcc Ni, fcc Ni-Cu alloy, bcc Fe, hcp Co, hcp Ti are 4.17 (4.08), 3.65 (3.59), 3.51 (3.50), 3.52 (3.54) , 2.83 (2.86),

a = 2.50, c = 4.00 (a = 2.50, c = 4.06), and a = 2.94, c = 4.64 (a = 2.95, c = 4.68) Å, respectively.[14–17] The lowest energy surface was modeled for each metal: Ag (111), Cu (111), Ni (111), Ni-Cu (111), Fe (110), Co (0001), Ti (0001).[18] A four-atomic-layer slab with (3 X 3) unit cell was used to represent each metal surface, corresponding to a surface coverage of 1/9 monolayer (ML). The adsorbates and the two topmost layers were allowed to relax, while the remaining layers were constrained. A plane wave energy cutoff of 400 eV was used with a 4 X 4 X 1 k-point set for all surfaces. Slabs are separated in the z direction with a vacuum spacing of 17 Å. Spin polarization and Methfessel-Paxton scheme[19] with energy smearing of 0.2 eV were applied for all calculations. Dipole corrections were included in the z direction to cancel out the net dipole moment on the surface and simulate the charge placed on the surface in electrochemical environment. Magnetic moment correction was applied for those metals that are ferromagnetic (Ni, Fe, Co).

Adsorption energies (E_{ads}) of nitric oxide and nitrite were calculated as

$$E_{ads} = E_{ads+slab} - E_{slab} - E_{ads_g} \quad [4]$$

where $E_{ads+slab}$ is the total energy of slab with the adsorbate, E_{slab} is the total energy of clean metal slab, and E_{ads_g} is the total energy of most stable configuration of adsorbate in gas phase. Free energies of adsorption were determined from DFT-calculated adsorption energies corrected with zero-point energy (ZPE) and standard state entropy corrections (T*S) using the harmonic oscillator approximation at 293K.

Activation barriers for nitric oxide dissociation on metal slabs were calculated using climbing image nudged elastic band (CI-NEB) method,[20–22] using six moving images between

the initial and final states. The calculations were considered convergence when the maximum residual force for adsorbate binding and CI-NEB were 0.02 and 0.05 eV/Å^{-2} respectively. Density of states calculations were performed with Blöchl corrections using the same energy cutoff with adsorption calculations and a gamma centered 4 X 4 X 1 k-point mesh.

2. Results

2.1. Cyclic voltammetry

CV of several TM foils in a series of $Na_xH_{3-x}PO_4$ concentrations illustrate a mass-transfer limited peak at potentials less-cathodic than the onset of water-dissociation mediated hydrogen evolution (Supplementary Figure 1). The magnitude of this mass-transfer limited peak, corresponding to phosphate-mediated hydrogen evolution, increases in concert with $Na_xH_{3-x}PO_4$ concentration, with peak potential becoming more cathodic as well. An anodic-going peak observed on Ni at *ca*. 0.2 V_{RHE}, corresponding to a combination of α-$Ni(OH)_2$ formation and hydride oxidation,[23,24] increases in magnitude with increasing $Na_xH_{3-x}PO_4$ concentration (Supplementary Figure 1b). This α-$Ni(OH)_2$ is then reduced in the cathodic-going sweep (see 10 mM $Na_xH_{3-x}PO_4$ in particular). Similarly, current in the double-layer capacitance region is shifted anodically (*ca*. 0.3 to 0.8 V_{RHE}), due to a combination of oxidation of residual dihydrogen near the electrode surface, hydride stripping, or further oxidation of α-$Ni(OH)_2$ to β-$Ni(OH)_2$.[23,24] The anodic-going extent of CVs for all other TMs were otherwise limited to avoid formation of surface oxide phases.[2]

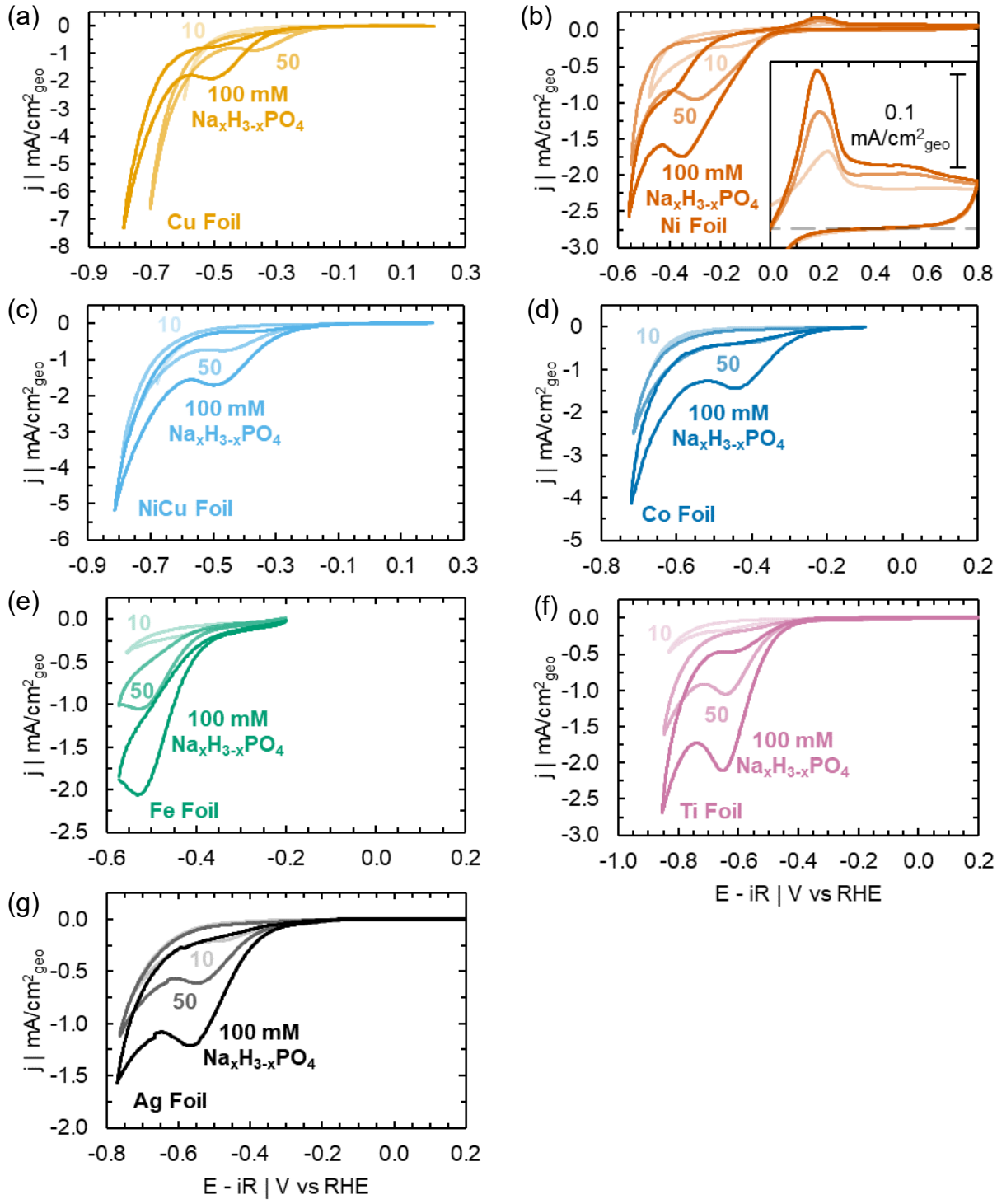

Supplementary Figure 1. CV collected at 10 mV/s for (a) Cu, (b) Ni, (c) $Ni_{0.68}Cu_{0.32}$, (d) Co, (e) Fe, (f) Ti, and (g) Ag foils at a series of quiescent $Na_xH_{3-x}PO_4$ concentrations (denoted). (b) Inset of the α-$Ni(OH)_2$ formation and stripping region with grey dashed line denoting 0 mA/cm^2_{geo}.

The mono- and di-basic phosphate anions comprising the $Na_xH_{3-x}PO_4$ buffer are

deprotonated at the electrode surface at potentials less-cathodic than water dissociation. These protons are then coupled to form dihydrogen. We confirm this by performing a simple rotating ring-disk electrode (RRDE) measurement in Ar-sparged 0.1 M $Na_xH_{3-x}PO_4$ with a Cu disk and Pt ring (Pine Research; Supplementary Figure 2). In the absence of rotation, a voltammetric profile similar to the polycrystalline foil in Supplementary Figure 1a is observed (Supplementary Figure 2a, black dashed trace). Current increases with increasing rotation rate (ω) at potentials cathodic of peak phosphate-mediated HER (Supplementary Figure 2a, ω increases with darker shades of red). Similarly, at the Pt ring, held at 0.7 V_{RHE} to oxidize produced dihydrogen, current increases with increasing ω with a potential-dependent profile comparable to that observed on the Cu disk. The ratio of ring to disk current (i_{Ring}/i_{Disk}) is comparable at potentials between *ca*. 0.6 and 0.8 V_{RHE}, indicating ω-independent ring collection efficiencies within this potential window.

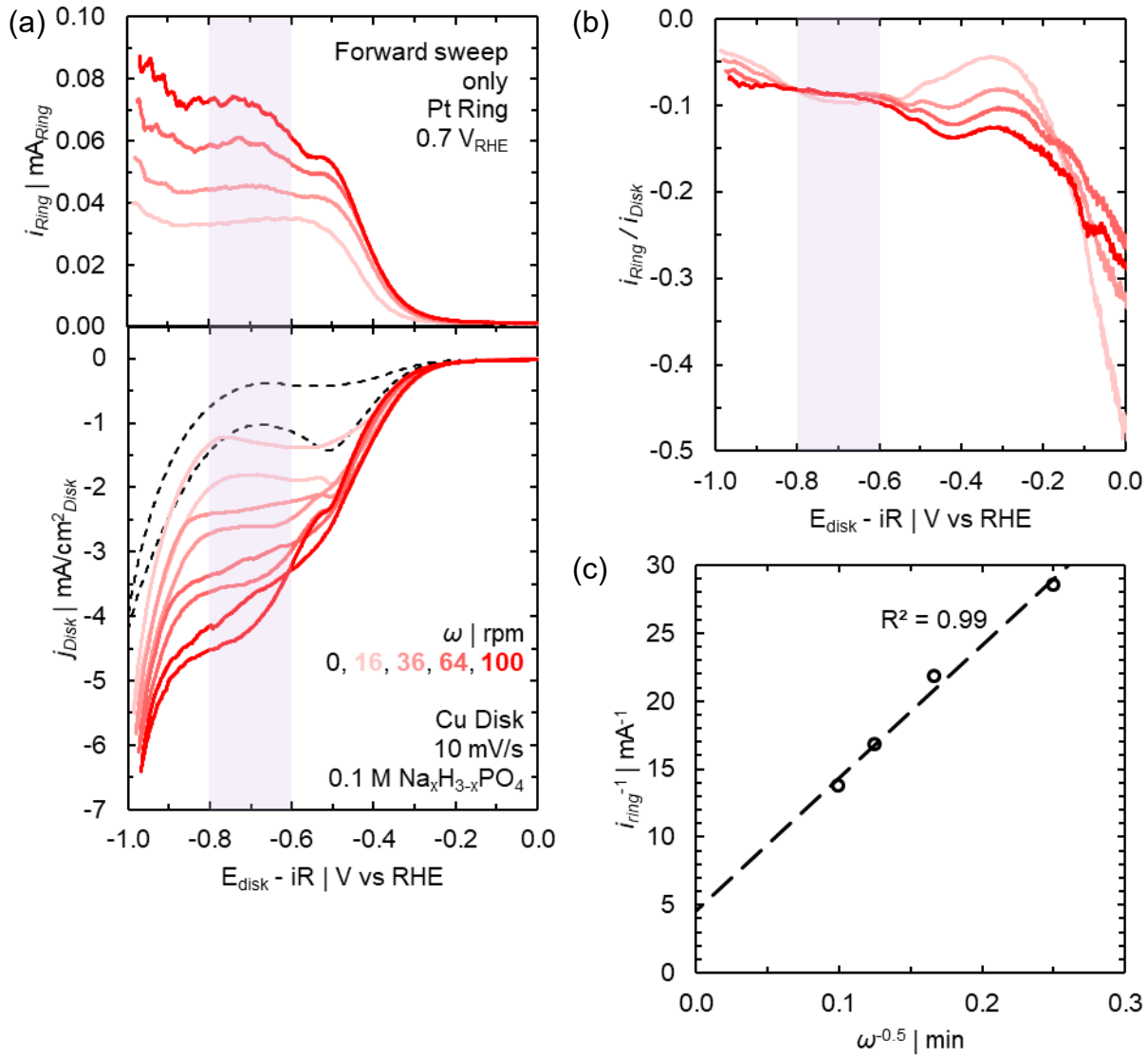

Supplementary Figure 2. (a) Rotating ring-disk electrode (RRDE) measurements performed in 0.1 M $Na_xH_{3-x}PO_4$ at on a Cu disk at 10 mV/s (bottom) while holding a Pt ring at 0.7 V_{RHE} (top) with rotation rates denoted. (b) Ratio of ring and disk currents (i_{Ring} / i_{Disk}) with transparent purple bar illustrating the range of potentials over which this ratio is independent of rotation rate and collection efficiencies are comparable for Levich analysis of i_{Ring}. Levich analysis of mass-transfer limited i_{Ring} indicates an electron transfer number of 1.6 ±0.25 e^-. This value assumes a saturated hydrogen concentration at 20 °C, where a ~20% less saturated solution results in the theoretical value of 2 e^-/H_2 oxidized. (c) Inverse average ring current (i_{ring}^{-1}) between 0.7 and 0.8 $V_{RHE,disk}$ vs ω^{-1}, providing the slope necessary to calculate the number of electrons transferred per phosphate-mediated HER turnover.

The linear correlation between the inverse of ring current (i_{Ring}), averaged from CV data points between 0.7 and 0.8 V_{RHE}, and $\omega^{-0.5}$ includes a non-zero intercept value, indicating

Koutecky-Levich analysis is necessary to extract the number of electrons transferred from phosphate-mediated HER. From the Koutecký-Levich equation,

$$\frac{1}{i} = \frac{1}{i_K} + \frac{1}{i_L} = \frac{1}{i_K} + \frac{1}{0.62nFA_{Ring}D^{2/3}\nu^{-1/6}[H_2]}\frac{1}{\omega^{1/2}} \quad [5]$$

where i_K is the kinetically-limited contribution to total current (i), and the mass-transfer limited contribution to current (i_L) can be expanded from the Levich equation, containing a dependence on $\omega^{-0.5}$. The number of electrons transferred during phosphate-mediated HER (n) can then be calculated from the slope of Supplementary Figure 2c as,

$$n = \frac{1}{\omega^{1/2}} \frac{1}{0.62FA_{Ring}D^{2/3}\nu^{-1/6}[H_2]\frac{d\left(i_{ring}^{-1}\right)}{d\left(\omega^{-1/2}\right)}} \frac{1}{\omega^{1/2}} \quad [6]$$

where F is Faraday's constant (96,485 C/mol-e$^-$), A_{Ring} is the area of the Pt ring (0.11 cm^2), D is the diffusion coefficient of dihydrogen in aqueous electrolyte (1.39x10^{-5} cm^2/s),[25] ν is the kinematic viscosity of the electrolyte (9.76x10^{-3} cm^2/s), hydrogen concentration $[H_2]$ is assumed to be saturated (780 μM H_2 at 20 °C), and $d\left(i_{ring}^{-1}\right)/d\left(\omega^{-1/2}\right)$ is the slope of inverse ring current versus inverse square root of rotate rate. From this analysis, an electron transfer number of 1.6 ±0.25 e$^-$/H_2 oxidized is determined. However, this assumes hydrogen concentration is saturated. Assuming hydrogen concentration is 80% of the saturated value yields an electron transfer number of 2.0, in-line with the theoretical electron transfer number for hydrogen oxidation. This lower than expected electron transfer number for hydrogen oxidation may also be caused by difficulties in assessing gas-phase reaction products via oxidation at a Pt ring.[26]

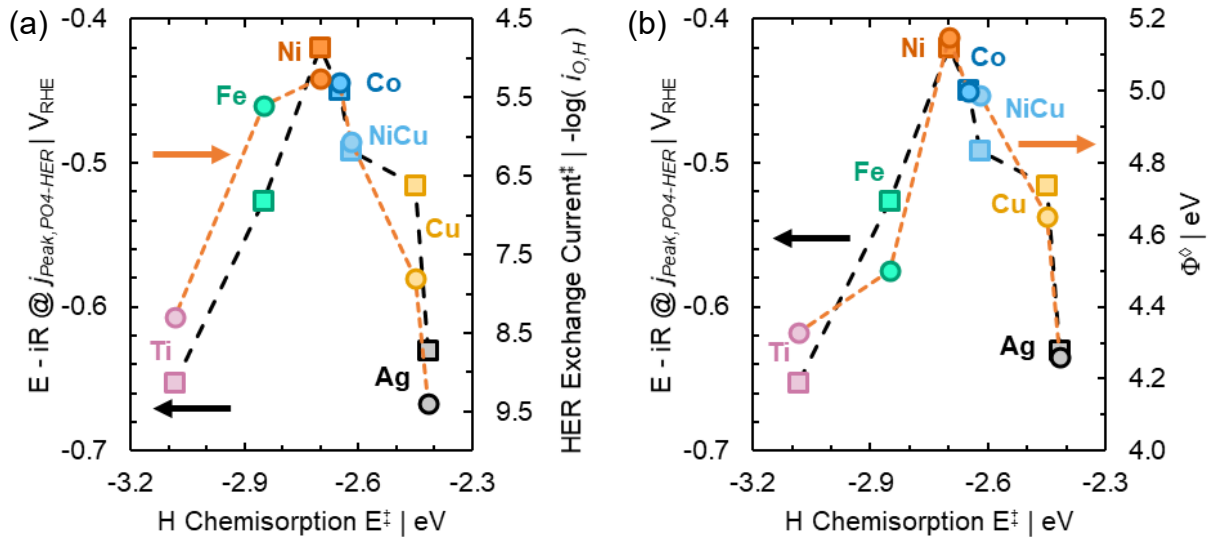

Supplementary Figure 3. E - iR @ $j_{Peak,PO4\text{-}HER}$ and work function$^{\lozenge}$ versus H chemisorption energy† for a series of TM foils, illustrating the Sabatier-like relationship between H chemisorption energy and metal work function and the utility of E – iR @ $j_{Peak,PO4\text{-}HER}$ in describing this relationship. Values for work function and H chemisorption energy of $Ni_{0.68}Cu_{0.32}$ alloy interpolated by mol fraction from literature values for Ni and Cu. $^{\lozenge\ddagger}$ Data for work function adapted from Ref. [27] and H chemisorption energy from Ref. [28].

Nitrate reduction current becomes apparent with increasing nitrate concentration at potentials less-cathodic than and including those where HER occurs (Supplementary Figure 4a-c and Figure 5a-d). Mass-transfer limited nitrate reduction is observed for certain TMs (e.g. Cu, Ni, $Ni_{0.68}Cu_{0.32}$, Co, Ti, and Ag), and identified as reduction of solution-phase reactants by observation of peaks giving way to increased current while performing CVs in 500-rpm stirred electrolyte (Supplementary Figure 4d-f and Figure 5e-h).

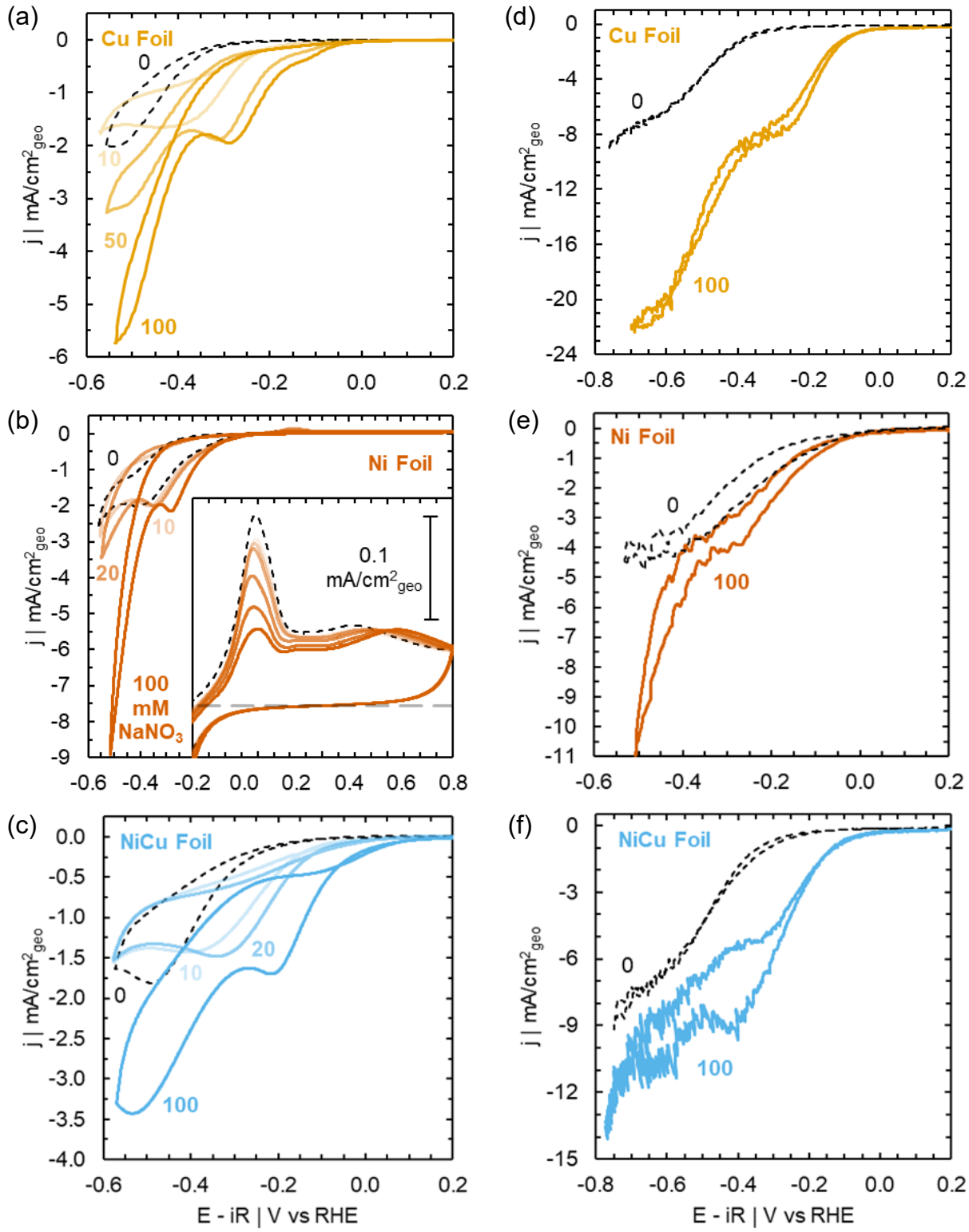

Supplementary Figure 4. CV collected at 10 mV/s for (a,d) Cu, (b,e) Ni, (c,f) $Ni_{0.68}Cu_{0.32}$ foils in quiescent (a-d) and 500-rpm stirred (e-h) 0.1 M $Na_xH_{3-x}PO_4$ with sodium nitrate concentration denoted. (b) Inset is of the NiO_x/α-$Ni(OH)_2$ formation and hydride oxidation region with grey dashed line denoting 0 mA/cm^2_{geo}.

In the interest of understanding the role of alloying on NO_3RR activity, we compare Cu and Ni catalysts with notable differences in HER and NO_3RR activity (Supplementary Figure 4). Cu, a poor HER electrocatalyst, is an active NO_3RR electrocatalyst in the neutral $Na_xH_{3-x}PO_4$ used here, consistent with literature in other electrolytes.[29–34] Current density for Ni, a good HER catalyst, in the presence of 0.1 M $NaNO_3$ increases appreciably at potentials cathodic of phosphate-mediated HER in both quiescent and 500-rpm stirred nitrate-containing electrolyte, though is less active than Cu in stirred electrolytes (Supplementary Figure 4). Alloying Cu with Ni ($Ni_{0.68}Cu_{0.32}$) shifts nitrate reduction onset to less-cathodic potentials than either pure monometal, in line with prior literature. As Wang et al. elude to, a shift in electronic structure (in particular E_d vs E_F) with alloying tunes intermediate adsorbate binding energies, resulting in enhanced activity of the alloy relative to either of its terminal contituents.[35] This observation agrees well with measurements made here, identifying optimal nitrate reduction activity at H chemisorption energies slightly weaker than that of Ni, and are in-line with recent literature explaining the enhanced alkaline HER activity of NiCu alloys.[36]

The magnitude of the anodic-going feature observed on Ni at *ca*. 0.2 V_{RHE} (likely from a mixture of α-$Ni(OH)_2$ formation and hydride stripping[23,24] attenuates with increasing nitrate concentration (Supplementary Figure 4b inset), indicating nitrate either interferes with formation of the α-$Ni(OH)_2$ by site blocking or consumes adsorbed hydrogen atoms that would otherwise be oxidized from the Ni surface. Quantitative measurement of nitrate-concentration dependent feature attenuation may provide a useful technique for characterizing adsorption thermodynamics for nitrate on Ni, as has recently been demonstrate when investigating organic

adsorption on Pt-group metals.[37–39]

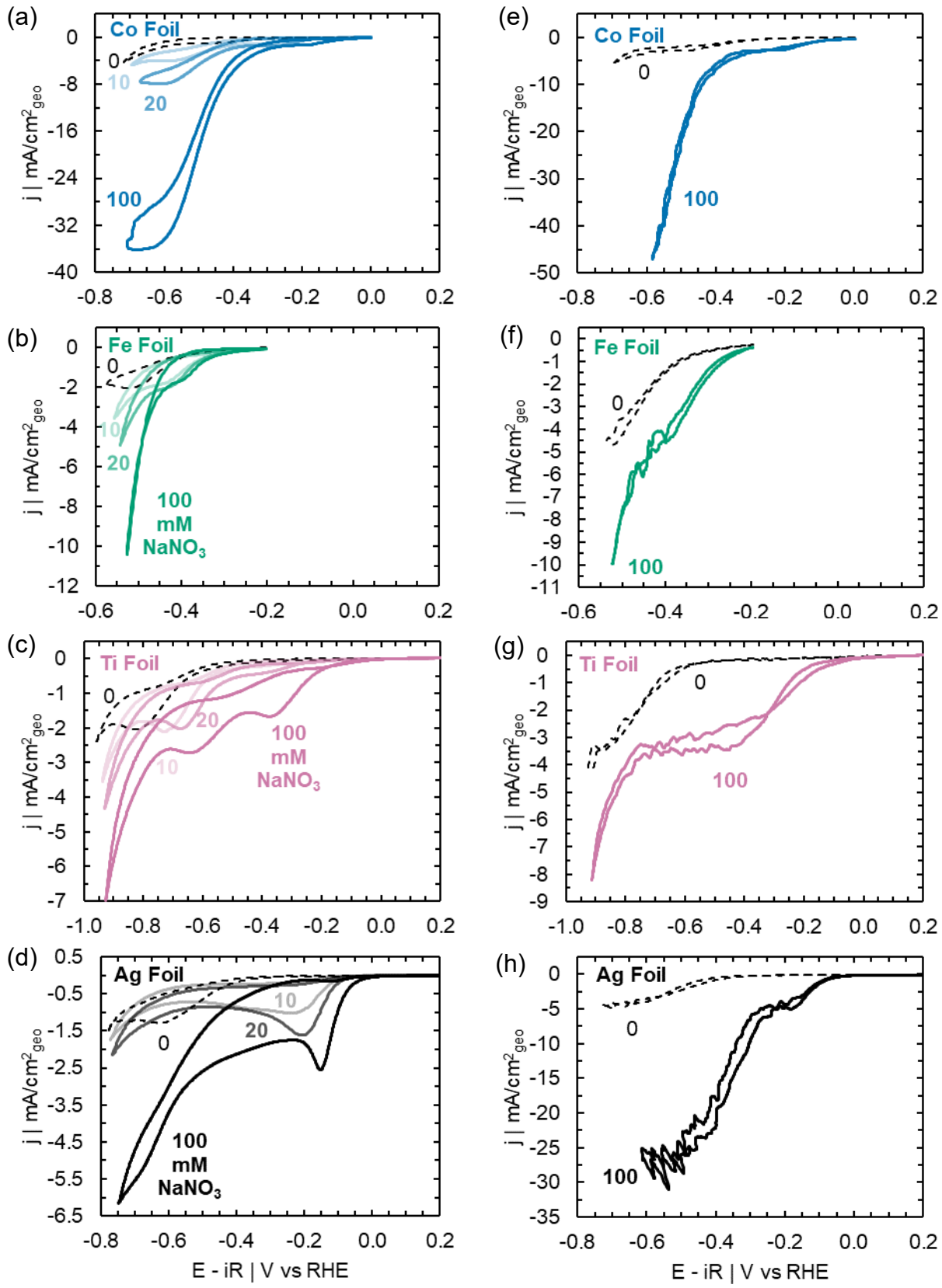

1 Supplementary Figure 5. CV collected at 10 mV/s for (a,e) Co, (b,f) Fe, (c,g) Ti, and (d,h) Ag foils in quiescent
2 (a-d) and 500-rpm stirred (e-h) 0.1 M $Na_xH_{3-x}PO_4$ with sodium nitrate concentration denoted in figure.

3

Considering the wider range of TMs investigated here (Figure 5), Co in particular demonstrates considerable activity in the presence of nitrate, even when compared to conventional benchmark monometals such as Cu and Ag. In 0.1 M $NaNO_3$, Co has an apparent NO_3RR onset that is less cathodic than either Ag or Cu and may be comparable to that of $Ni_{0.68}Cu_{0.32}$. (A direct comparison between $Ni_{0.68}Cu_{0.32}$ and Co onset potentials is challenging, as Co was not exposed to potentials > 0 V_{RHE} to avoid oxide formation.) Similarly, the potential at mass-transfer limited nitrate reduction for Co is second only to Ag of the TMs along the weak H chemisorption energy arm (circles in Figure 1a,c). Perhaps most impressively is the current density produced by Co at comparable potentials to other benchmark electrocatalysts, producing roughly twice the current density of Cu and Ag in 500-rpm stirred electrolyte at -0.6 V_{RHE} (Supplementary Figure 4 and Figure 5).

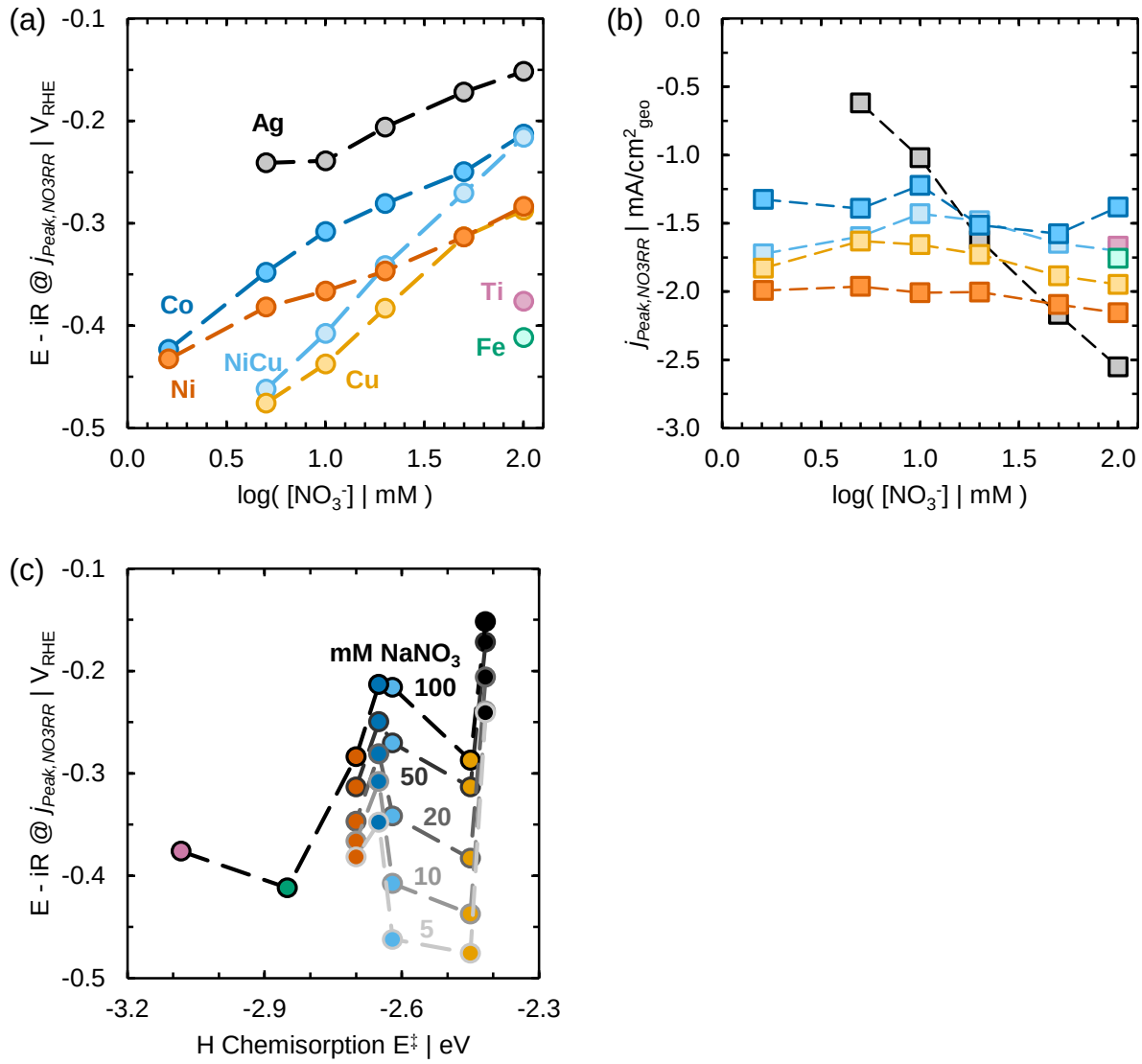

Supplementary Figure 6. (a) Potential and (b) current at mass-transfer limited nitrate reduction, measured by CV in 0.1 M $Na_xH_{3-x}PO_4$ at 10 mV/s (Supplementary Figure 4 and Figure 5), against logarithmic nitrate concentration for Ag (black), Cu (golden), $Ni_{0.68}Cu_{0.32}$ (light blue), Co (dark blue), Ni (orange), Fe (green), and Ti (pink). Points for Fe and Co at 0.1 M $NaNO_3$ ($\log[NO_3^-] = 2.0$) determined as inflection point (minimum in differential current with respect to voltage). (c) Potential at mass-transfer limited nitrate reduction for the same TM foils and in same conditions as in (a) and (b) plotted against H chemisorption energy from Ref. [28], with nitrate concentrations denoted in mM.

Mass-transfer limited features shift to less-cathodic potentials with increasing logarithmic nitrate concentration (Supplementary Figure 6a), where the Nernst equation bears a linear dependence on the logarithmic ratio of reactants and products (Supplementary equation 31).

However, mass-transfer limited currents are nominally independent of nitrate concentrations, with the exception of Ag (Supplementary Figure 6b). For 3d TMs, the comparable current densities between mass-transfer limited features in the absence (black dashed lines) and presence of nitrate (solid lines, Supplementary Figure 4 and Figure 5) indicates these are likely bound by phosphate diffusion.

2.2. Nitrate reaction rate order and microkinetic model

2.2.1. Steady-state CA

Steady-state current density was measured by chronoamperometry (steady-state CA) for 30 s each at 40 mV increments across a range of potentials in 500-rpm stirred 0.1 M $Na_xH_{3-x}PO_4$ with a series of sodium nitrate concentrations (Figure 7). Select TMs, particularly those with H chemisorption energies weaker than that of Ni (e.g. Cu, $Ni_{0.68}Cu_{0.32}$, Co, and Ag), demonstrate appreciable nitrate reduction activity illustrated by increasing logarithmic current density at a fixed potential with increasing nitrate concentration. All TMs appear to demonstrate mass-transfer limitations as current density approaches ~10 mA/cm^2_{geo} ($\log(-j \mid mA/cm^2_{geo}) = 1.0$), evidenced by a plateau in logarithmic current with increasing potential. However, Co begins to overcome this mass-transfer limitation in 100 mM $NaNO_3$ by -0.4 V_{RHE}, continuing to increase and approaching values of ~100 mA/cm^2_{geo} ($\log(-j \mid mA/cm^2_{geo}) = 2.0$) by -0.55 V_{RHE}. This behavior suggests that the initial mass-transfer limitation at ~ 10 mA/cm^2_{geo} is caused by phosphate anion concentration, and that initial mass-transfer limitations can be overcome as water dissociation begins to supply protons.

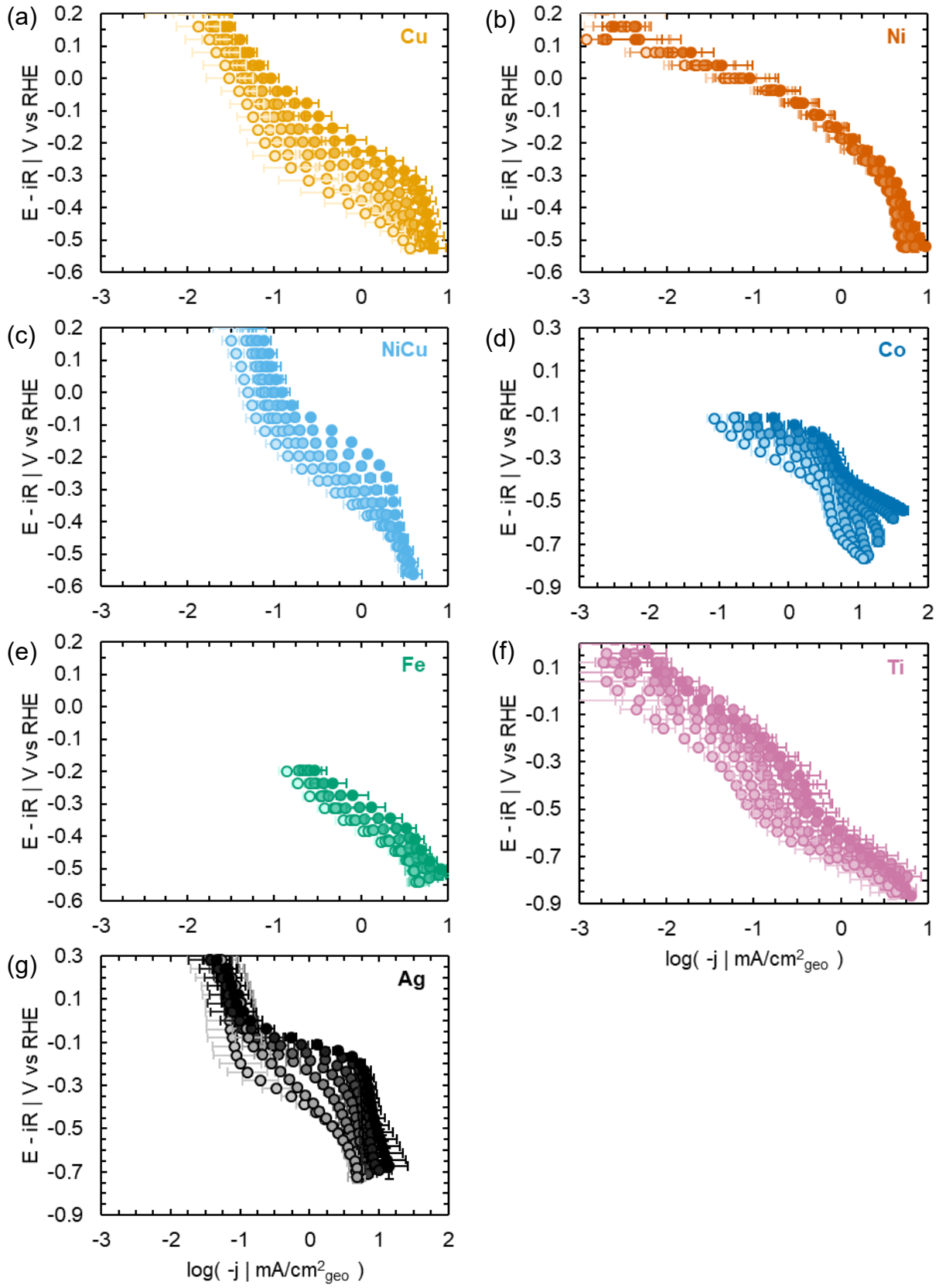

Supplementary Figure 7. Steady-state CA collected in 500-rpm stirred 0.1 M $Na_xH_{3-x}PO_4$ with a series of nitrate concentrations (0, 1.6, 6, 10, 20, 50, and 100 mM with increasingly dark shades) at 40 mV increments for (a) Cu, (b) Ni, (c) $Ni_{0.68}Cu_{0.32}$, (d) Co, (e) Fe, (f) Ti, and (g) Ag foils.

Nitrate reduction rate order is then interpreted assuming Butler-Volmer kinetics as the slope of logarithmic current density against logarithmic nitrate concentration at fixed applied potential (Supplementary Figure 8 and Supplementary Figure 9). A distinct bell-shaped nitrate rate order profile is apparent for TMs corresponding to the weak binding arm (e.g. Ag, Cu, $Ni_{0.68}Cu_{0.32}$, and Co) of the Sabatier-like relationship between H chemisorption energy and HER activity (Supplementary Figure 3). Conversely, TMs on the strong-binding arm (e.g. Fe and Ti) nitrate rate order peaks are generally lower in magnitude and nominally less discrete than for those on the weak-binding arm. We note that the bi-modal distribution of rate order observed on metals with high selectivity towards ammonium (i.e. those consuming a large number of protons such as Co and Fe) may actually be due to phosphate anion mass-transfer limitations in the 500-rpm stirred electrolyte used here for steady-state CA. This can also be observed in the pinch-point of steady-state CA data for Co at *ca*. -0.45 V_{RHE}, where current plateaus before once again increasing exponentially with the onset of water dissociation as a source of protons (see discussion of Figure 7 in prior paragraph).

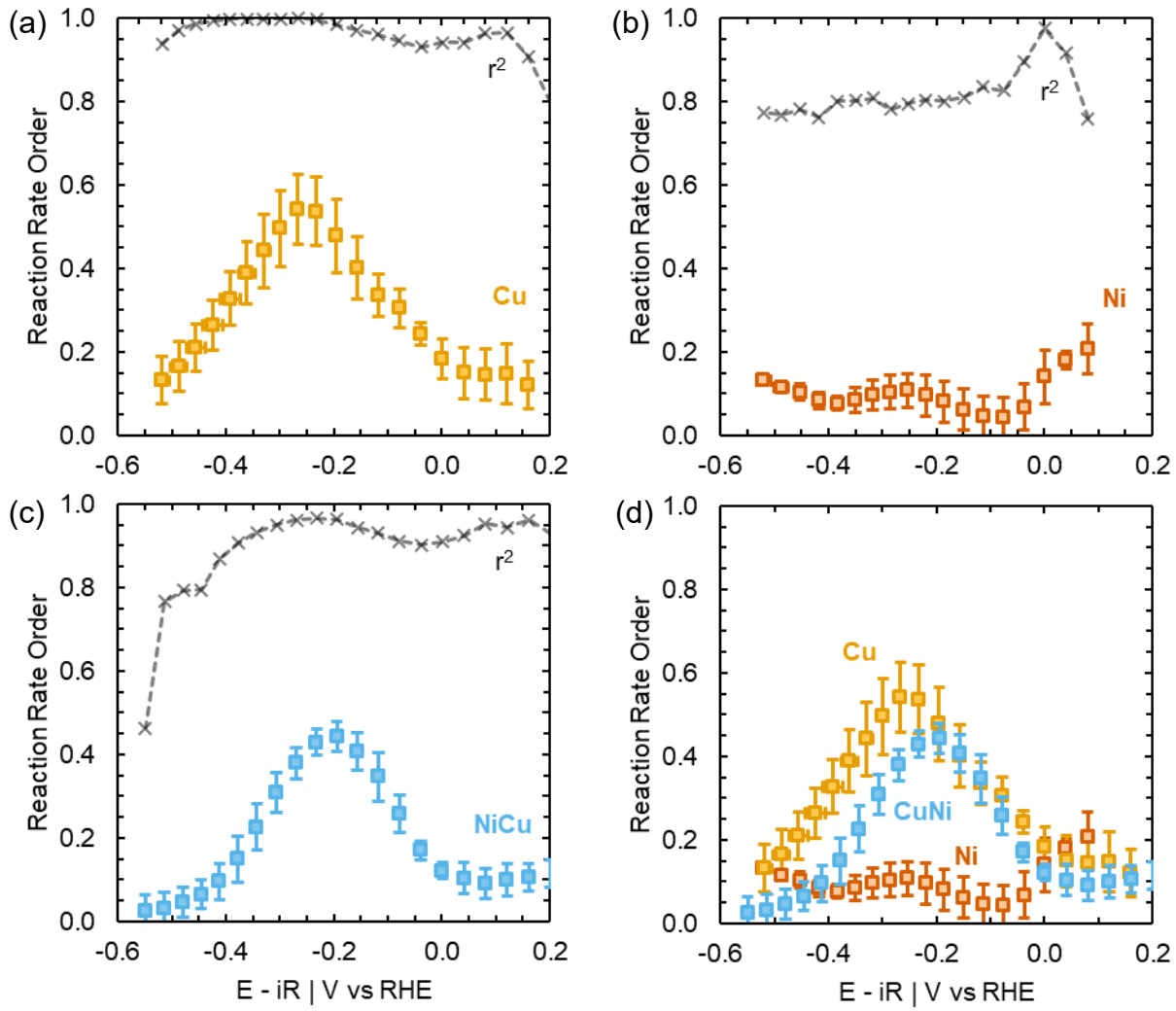

Supplementary Figure 8. NO_3RR order as a function of applied potential for (a) Cu, (b) Ni, and (c) $Ni_{0.68}Cu_{0.32}$ foils plotted separately and plotted together as (d) for comparison. Coefficient of determination (r^2) values for individual foils are derived from the linear regression of average values from three (n = 3) separate measurements. Error bars denote plus and minus one standard deviation from the average of at least three (n = 3) separate measurements.

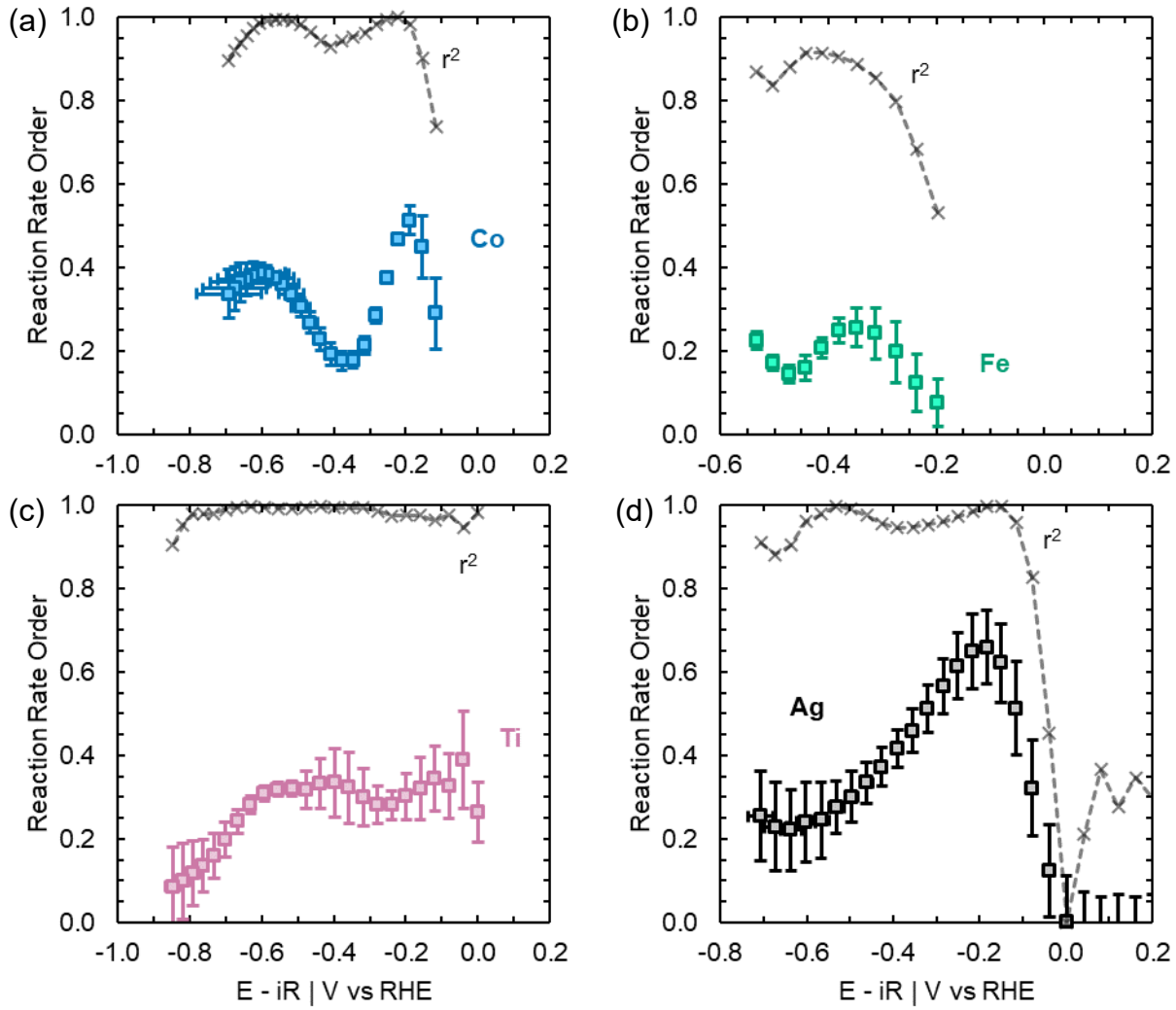

Supplementary Figure 9. NO_3RR order as a function of applied potential for (a) Co, (b) Fe, (c) Ti, and (d) Ag foils plotted separately. Coefficient of determination (r^2) values for individual foils are derived from the linear regression of average values from three (n = 3) separate measurements. Error bars denote plus and minus one standard deviation from the average of at least three (n = 3) separate measurements.

2.2.2. Microkinetic model

We hypothesize that competition between H^* and nitrate anions for adsorption sites, and subsequent reduction in the HER and NO_3RR, play a role in dictating rate order. We investigate this hypothesis by developing a microkinetic model, capturing well the potential-dependent nitrate rate order profile. We begin by describing the elementary steps, potential-dependent

coverage, and kinetics of the HER, following the work of Shinagawa *et al*.[40] We then extend this microkinetic model of the HER to include NO_3RR in a competitive Langmuir-Hinshelwood model, where H^* and nitrate anions compete for adsorption sites. In this model we neglect all mass-transfer effects, assuming the local reactant activity in the reactive Helmholtz plane is equivalent to that of the bulk electrolyte.

The reduction of protons (H^+) into hydrogen gas (H_2) by the HER generally consists of three potential mechanistic steps:

$$H^+ + * + e^- \leftrightarrow H^* \quad [7]$$

$$H^* + H^+ + e^- \leftrightarrow H_2 + * \quad [8]$$

$$H^* + H^* \leftrightarrow H_2 + 2* \quad [9]$$

where $*$ denotes a surface site available for proton adsorption, and H^* denotes an adsorbed hydrogen atom after accepting an electron (e^-). If Supplementary equation 7, referred to as the Volmer step, is rate-limiting,

$$r_1 = k_{1F}\alpha_{H^+}\theta_* \quad [10]$$

where α_{H^+} is the activity of protons, assumed to be equivalent to the concentration of phosphate buffer here (0.1 M $Na_xH_{3-x}PO_4$), θ_* is the fraction of unoccupied surface sites, and k_{1F} is the forward reaction rate constant. Because the Volmer step involves an electron-transfer step, k_{1F} bears a dependence on applied potential, and Supplementary equation 10 can be expanded to,

$$r_1 = k_{1F}^0\alpha_{H^+}\left(1 - \theta_{NO_3^-} - \theta_H\right)\exp[-\alpha f\eta_1] \quad [11]$$

where θ_* has also be expanded to include the fractional coverage of nitrate $\left(\theta_{NO_3^-}\right)$ and H^*

(θ_H), α is the electron transfer coefficient (defined here as 0.21 to reflect typical nitrate reduction Tafel slopes of 120 mV/dec), f denotes the ratio between Faraday's constant and the product of the gas constant and temperature (F/RT), and η_1 is overpotential.

Alternatively, if either Supplementary equation 8 or 9 are rate-limiting, Supplementary equation 7 becomes quasi-equilibrated and the forward and reverse rates are equivalent,

$$r_{1,eq} = 0 = k_{1F}\alpha_{H^+}\left(1 - \theta_{NO_3^-} - \theta_H\right) - k_{1R}\theta_H \quad [12]$$

where k_{1R} also bears a potential dependence as $k_{1R}^0 \exp\left[(1-\alpha)f\eta_1\right]$. The potential-dependent fractional coverage of H* can then be determined as,

$$\theta_H = \frac{K_H\alpha_{H^+}\left(1-\theta_{NO_3^-}\right)}{\exp[f\eta_1]+K_H\alpha_{H^+}} \quad [13]$$

where K_H is the equilibrium adsorption coefficient of H*, equivalent to the ratio of forward and reverse rate constants at equilibrium (k_{1F}/k_{1R}). Supplementary equation 13 allows derivation of rate equations for the Heyrovsky step,

$$r_2 = k_{2F}^0\alpha_{H^+}\theta_H \exp[-\alpha f\eta_2] \quad [14]$$

and for the Tafel step,

$$r_3 = k_{3F}^0\theta_H^2 \quad [15]$$

where the Tafel step does not include any electron transfer, and is therefore potential-independent.

Prior literature has identified the rate-limiting step of electrochemical nitrate reduction as the conversion of adsorbed nitrate to nitrite.[29,31,41–46] Because the rate-limiting step of nitrate reduction is proposed to occur after adsorption of nitrate,

$$NO_3^- + * \leftrightarrow NO_3^{-*} \quad [16]$$

the adsorption of nitrate is then quasi-equilibrated. The ratio of potential-independent forward and reverse reaction rate constants (k_{4F}/k_{4R}),

$$r_{4,eq} = 0 = k_{4F}\alpha_{NO_3^-}\left(1 - \theta_{NO_3^-} - \theta_H\right) - k_{4R}\theta_{NO_3^-} \quad [17]$$

is equal to the nitrate adsorption coefficient $\left(K_{NO_3^-}\right)$. Solving this expression for $\theta_{NO_3^-}$,

$$\theta_{NO_3^-} = \frac{K_{NO_3^-}\alpha_{NO_3^-}(1-\theta_H)}{1+K_{NO_3^-}\alpha_{NO_3^-}} \quad [18]$$

provides the familiar competitive Langmuir-Hinshelwood model for nitrate coverage.

Nitrate coverage (Supplementary equation 18) is not explicitly treated as potential-dependent here, but rather captures potential-dependence implicitly by including H* and nitrate anions as competing adsorbates in a Langmuir adsorption isotherm. Under increasingly cathodic potential, the onset of H* coverage occurs and nitrate anions are displaced. The potential at which H* coverage overcomes that of nitrate anions shifts to increasingly less-cathodic potentials with the logarithmic ratio of H* to nitrate adsorption coefficients ($K_H/K_{NO_3^-}$, related to free energy as $\Delta G_{H*} - \Delta G_{NO_3^-*} \propto -\ln(K_H/K_{NO_3^-})$, Supplementary Figure 10).

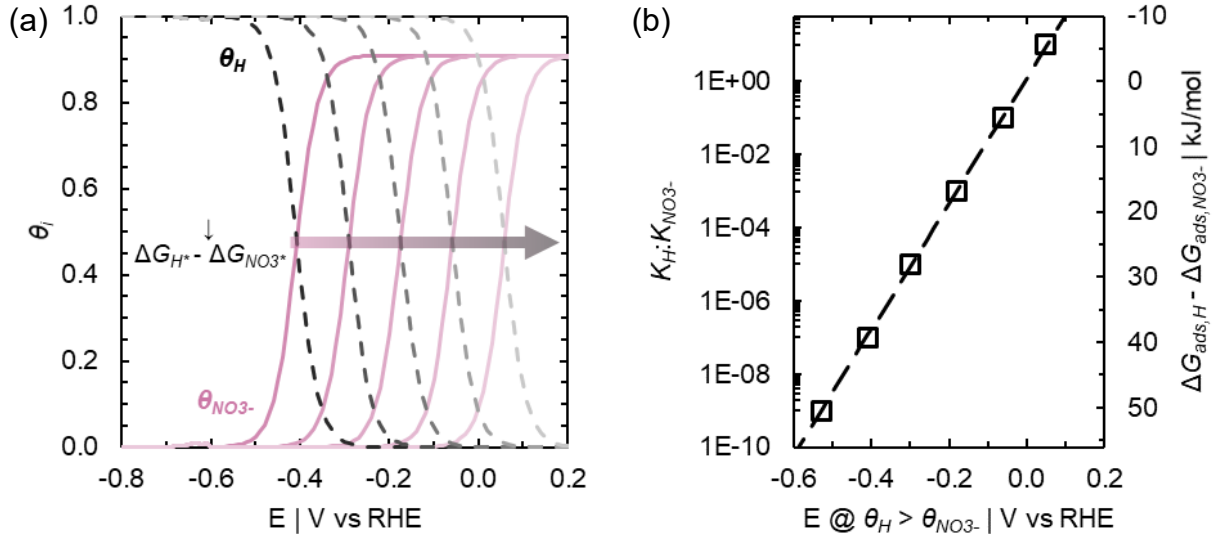

Supplementary Figure 10. (a) Potential-dependent fractional H* (shades of black) and nitrate (shades of fuchsia) coverage for a series of H* to nitrate adsorption coefficients ($K_H/K_{NO_3^-}$) denoted by increasingly light shades in order of 10^{-9}, 10^{-7}, 10^{-5}, 10^{-3}, 10^{-1}, and 10^{1}. (b) $K_H/K_{NO_3^-}$ demonstrates a linear trends as a function of the potential at which H* coverage exceeds nitrate coverage (E @ $\theta_H > \theta_{NO_3^-}$), while the trend is linear for H* free energy of adsorption relative to that of nitrate ($\Delta G_{H*} - \Delta G_{NO_3^-*}$).

In contrast, nitrate anion coverage at sufficiently non-cathodic potentials (well away from the onset of increasing H* coverage) is solely dependent on nitrate activity (assumed equal to concentration here [NO_3^-]) and adsorption coefficient ($K_{NO_3^-}$; Supplementary Figure 11a). At low nitrate concentration, nitrate coverage scales linearly with nitrate concentration (Supplementary Figure 11b). At sufficiently high nitrate concentrations to approach saturation the relationship between nitrate coverage and concentration becomes non-linear, in-line with conventional Langmuir adsorption isotherms. Nitrate coverage scales monotonically with $K_{NO_3^-}$ within the nominally zero H* coverage regime (Supplementary Figure 11c).

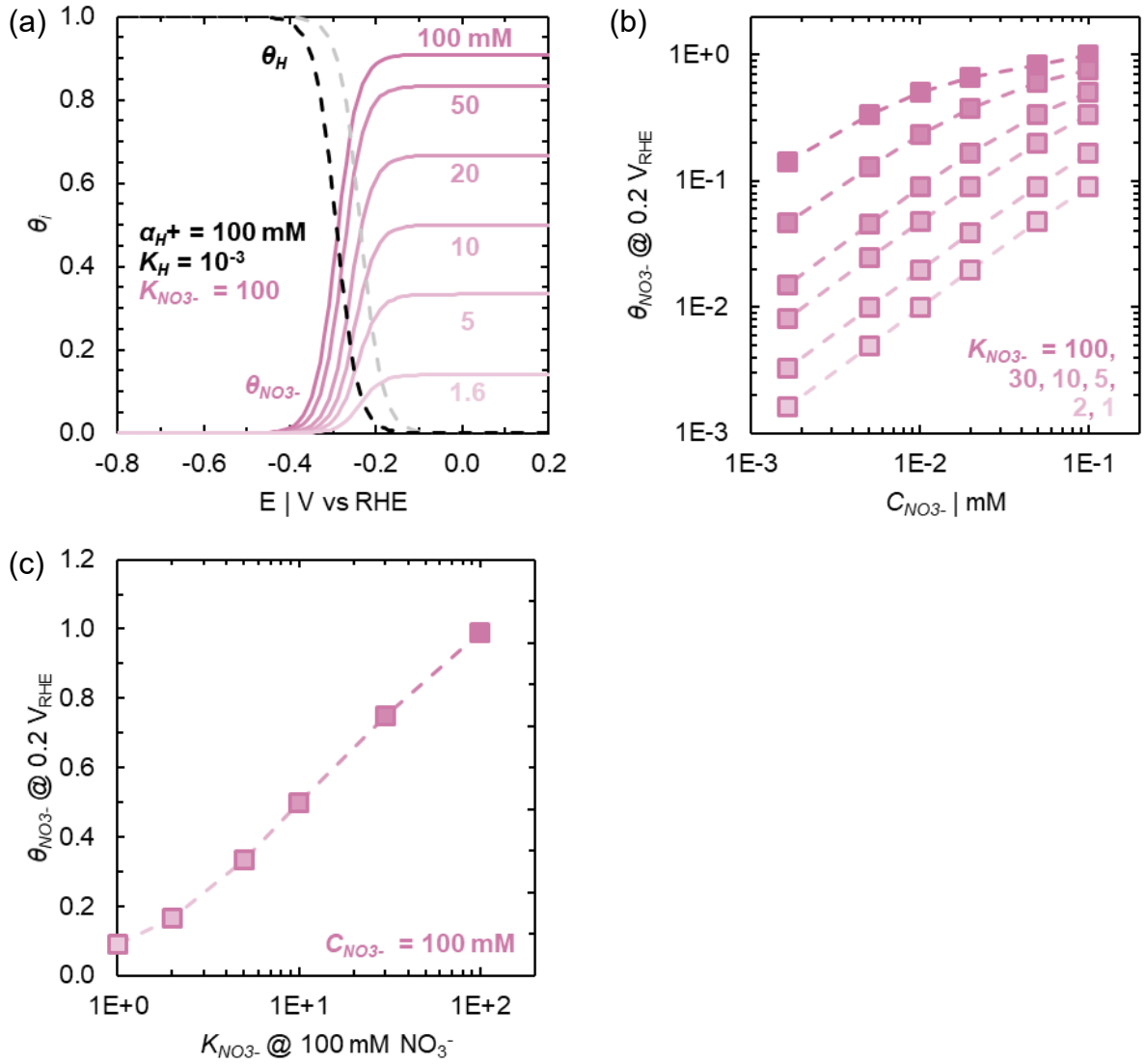

Supplementary Figure 11. (a) Potential-dependent nitrate coverage depends on H* coverage (and consequently α_{H^+} and K_H), (b) $\alpha_{NO_3^-}$, and (b,c) $K_{NO_3^-}$.

We then propose that rate-limiting nitrate reduction proceeds by one of three mechanisms and rate expressions: (1) a Heyrovsky-like (Eley-Rideal),

$$NO_3^{-*} + 2H^+ + 2e^- \leftrightarrow NO_2^{-*} + H_2O \quad [19]$$

$$r_5 = k_{5F}^0 \alpha_{H^+}^2 \theta_{NO_3^-} \exp[-\alpha f \eta_5]$$

(2) a Tafel-like (Langmuir-Hinshelwood),

$$NO_3^{-*} + 2H^* \leftrightarrow NO_2^{-*} + H_2O + 2* \quad [20]$$

$$r_6 = k_{6F}^0 \theta_H^2 \theta_{NO_3^-}$$

or (3) a mixed mechanism,

$$NO_3^{-*} + H^+ + H^* + e^- \leftrightarrow NO_2^{-*} + H_2O + * \quad [21]$$

$$r_7 = k_{7F}^0 \alpha_{H^+} \theta_H \theta_{NO_3^-} \exp[-\alpha f \eta_7]$$

where Supplementary equations 19 and 21 provide potential-dependent NO_3RR kinetics, while the kinetics of Supplementary equation 20 are implicitly potential dependent (not involving a charge-transfer step) due to proportionality with potential-dependent nitrate coverage (Supplementary equation 18). Nitrite is then assumed to reduce rapidly or desorb from the surface at sufficient rate that its coverage is negligible and may be disregarded. Current density (j_i) corresponding to a specific reaction mechanism (i) is then expressed as

$$j_i = n_i F r_i \quad [22]$$

where n_i is the number of electrons transferred per reaction (e.g. conversion of nitrate to a given product). Combining Supplementary equations 11, 13-15, and 18-22 provides the equations describing current for the HER,

$$\text{(Volmer)} \qquad j_1 = n_1 F k_{1F}^0 \alpha_{H^+} \left(1 - \theta_H - \theta_{NO_3^-}\right) \exp[-\alpha f \eta_1] \quad [23]$$

$$\text{(Heyrovsky)} \qquad j_2 = n_2 F k_{2F}^0 \alpha_{H^+} \theta_H \exp[-\alpha f \eta_2] \quad [24]$$

$$\text{(Tafel)} \qquad j_3 = n_3 F k_{3F}^0 \theta_H^2 \quad [25]$$

and for the NO_3RR,

$$\text{(Eley-Rideal)} \qquad j_5 = n_5 F k_{5F}^0 \theta_{NO_3^-} \alpha_{H^+}^2 \exp[-\alpha f \eta_5] \quad [26]$$

$$\text{(Langmuir-Hinshelwood)} \qquad j_6 = n_6 F k_{6F}^0 \theta_{NO_3^-} \theta_H^2 \quad [27]$$

(Mixed) $$j_7 = n_7 F k_{7F}^0 \theta_{NO_3^-} \theta_H \alpha_{H^+} \exp[-\alpha f \eta_7] \quad [28]$$

where $n_1 = n_2 = n_3 = 2\ e^-$ to reflect 2 e^-/H_2 produced, and n_5, n_6, and n_7 range between 2 and 8 e^-/NO_3^- reduced. This treatment of n_{NO_3RR} (n_5, n_6, n_7) allows the derived microkinetic model to describe reaction rate, while the experimentally-measured current is then described by inclusion of material- and potential-dependent selectivity (Figures S16 and S17 and Supplementary Table 2).

Overpotential is defined as the potential difference between the onset potential (η_0) and applied potential. For the HER, $\eta_{0,HER}$ is defined simply as 0 V vs the reversible hydrogen electrode (RHE), such that $\eta_1 = \eta_2 = E_{applied}$. Alternatively, η_{0,NO_3RR} is defined as the reduction potential of the rate-limiting step,[47–49]

$$NO_3^- + H_2O + 2e^- \overset{0.01\ V_{SHE}}{\longleftrightarrow} NO_2^- + 2OH^- \quad [29]$$

as 0.01 V vs the standard hydrogen electrode (SHE) where nitrate reduces to nitrite at pH where nitrite forms deprotonated (pH > pK_a). While this equilibrium is written to occur in alkaline conditions (pH 14),[49] in-line with the included citation, we assume protons reduce to water rather than water reduction to hydroxide ions. We then correct the SHE potential to the RHE potential by the Nernst equation,[50]

$$E = E^0 - \frac{RT}{nF\log(e)} \log\left[\frac{\alpha_{NO_2^-}}{\alpha_{NO_3^-}\alpha_{H^+}^2}\right] \quad [30]$$

which contains the ratio of activity coefficients for products $\left(\alpha_{NO_2^-}\right)$ and reactants $(\alpha_{NO_3^-}, \alpha_{H^+}^2)$ of the rate-limiting step described in 29. Assuming a temperature of 293 K, $n = 2$, activity coefficients as equivalent to concentration, and the definition of pH as $-\log[H^+]$,

$$E = E^0 + pH\frac{2RT}{nF\log(e)} + \frac{2RT}{nF\log(e)} \log\frac{[NO_3^-]}{[NO_2^-]} \quad [31]$$

which allows the potential to be corrected for pH. While the ratio of nitrate to product activities (final term of Supplementary equation 31) does dictate onset potential (Supplementary Figure 4 and Figure 5),[6] we neglect it here as local product activity and composition is poorly defined and its value does not affect the adsorption of nitrate in our model or the nitrate rate order profile observed. Therefore, at pH 7, the redox potential used to describe the equilibrium between nitrate and nitrite is η_{0,NO_3RR} =0.84 V vs RHE.[47]

To better understand the behavior of these different mechanisms for rate-limiting step, Supplementary Figure 12 provides the potential-dependent reaction rate for each of the proposed steps in the (a) HER and (b) NO_3RR on a surface with low H^* affinity. HER rate does not become appreciable until the onset of H^* coverage; however, at H^* coverages approaching zero Volmer-limited HER (r_1) does provide some initial rate. The Eley-Rideal like Heyrovsky step (r_2) undergoes an exponential rate increase in concert with H^* coverage. Tafel step (r_3) rate increases with H^* coverage, plateauing as H^* coverage approaches unity. Despite having the same reaction rate constants (k_{iF}^0) and electron transfer units (α) for this example, the Heyrovsky step (r_2) dominates the overall HER rate. This behavior is reflective of the model we use to elucidate the mechanistic interpretation of nitrate rate order in the main text.

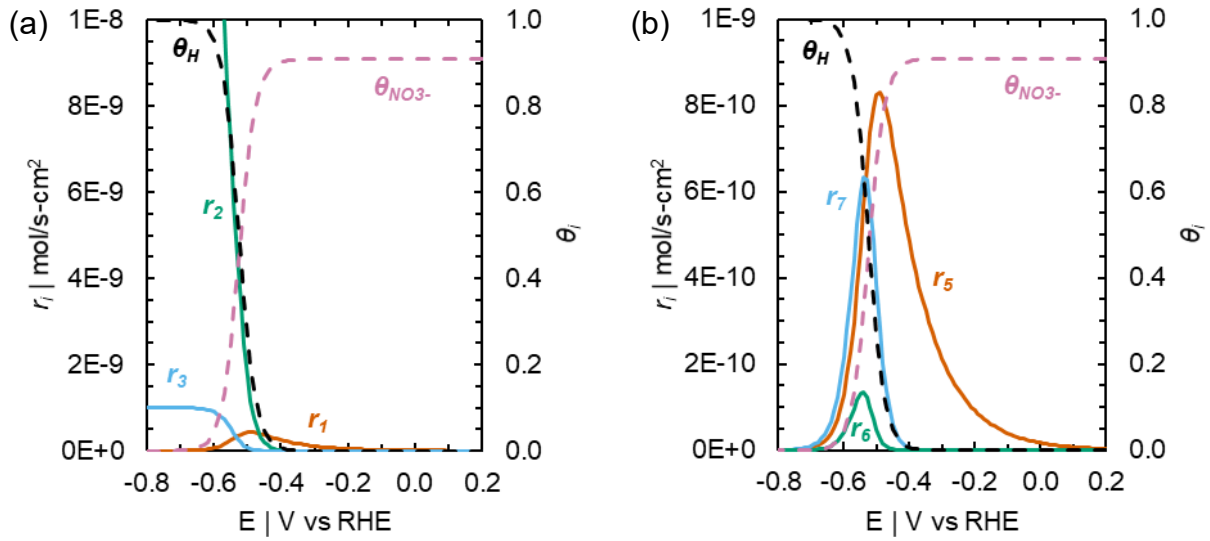

Supplementary Figure 12. Potential-dependent reaction rates of (a) HER and (b) NO_3RR mechanistic rate-limiting steps and H* (black dashed) and nitrate (fuchsia dashes) fractional coverage for a low H*-affinity case where K_H =10^{-7}, $K_{NO_3^-}$ =10^2, α_{H^+} =0.1 M, $\alpha_{NO_3^-}$ =0.1 M, α =0.21 for all steps, n_i =2e$^-$ for all steps for simplicity, k_{1F}^0 =10^{-9} L/s-cm^2, k_{2F}^0 =10^{-9} L/s-cm^2, k_{3F}^0 =10^{-9} mol/s-cm^2, k_{5F}^0 =2.0x10^{-12} L^2/mol-s-cm^2, k_{6F}^0 =3.5x10^{-13} mol/s-cm^2, and k_{7F}^0 =10^{-9} L/s-cm^2.

In the case of the NO_3RR (Supplementary Figure 12b), total reaction rate increases at potentials less-cathodic than the onset of H* coverage, reaches a maximum at intermediate H* coverage, and then approaches zero as H* coverage approaches saturation. The purely Eley-Rideal step (r_5), involving two proton-coupled electron transfer steps from solution-phase protons, provides nitrate reduction rate at less-cathodic potentials where H* coverage is negligible. In concert with the onset of H* coverage (Supplementary Figure 12), the rate of purely Langmuir-Hinshelwood and mixed (Supplementary equations 20 and 21) nitrate reduction steps increase, while the Eley-Rideal like rate peaks and decreases. As H* coverage overcomes that of nitrate, the rate of surface-mediated nitrate reduction steps (Supplementary equations 20 and 21) peak and decrease. Because mass-transfer limitations are neglected, the rate of all nitrate reduction steps approach zero as H* coverage approaches unity, displacing

adsorbed nitrate.

As we discuss in the main text (Figure 2), this ratio of thermodynamic parameters ($\Delta G_{H*} - \Delta G_{NO_3^-*} \propto -\ln [K_{H^+}/K_{NO_3^-}]$) plays a major role in dictating the shape (peak location and magnitude) of nitrate rate order. As $G_{H*} - \Delta G_{NO_3^-*}$decreases, the magnitude of nitrate rate order decreases and the peak potential shifts to less-cathodic potentials (Supplementary Figure 13a). This can be explained by the exponential dependence of the Butler-Volmer nitrate reduction kinetics used here on applied potential. Peak rate order increases nominally exponentially with $G_{H*} - \Delta G_{NO_3^-*}$; however, at the highest H* affinities (most negative $G_{H*} - \Delta G_{NO_3^-*}$) this trend no longer holds (Supplementary Figure 13c), and peak rate order decreases to below the expected exponential trend.

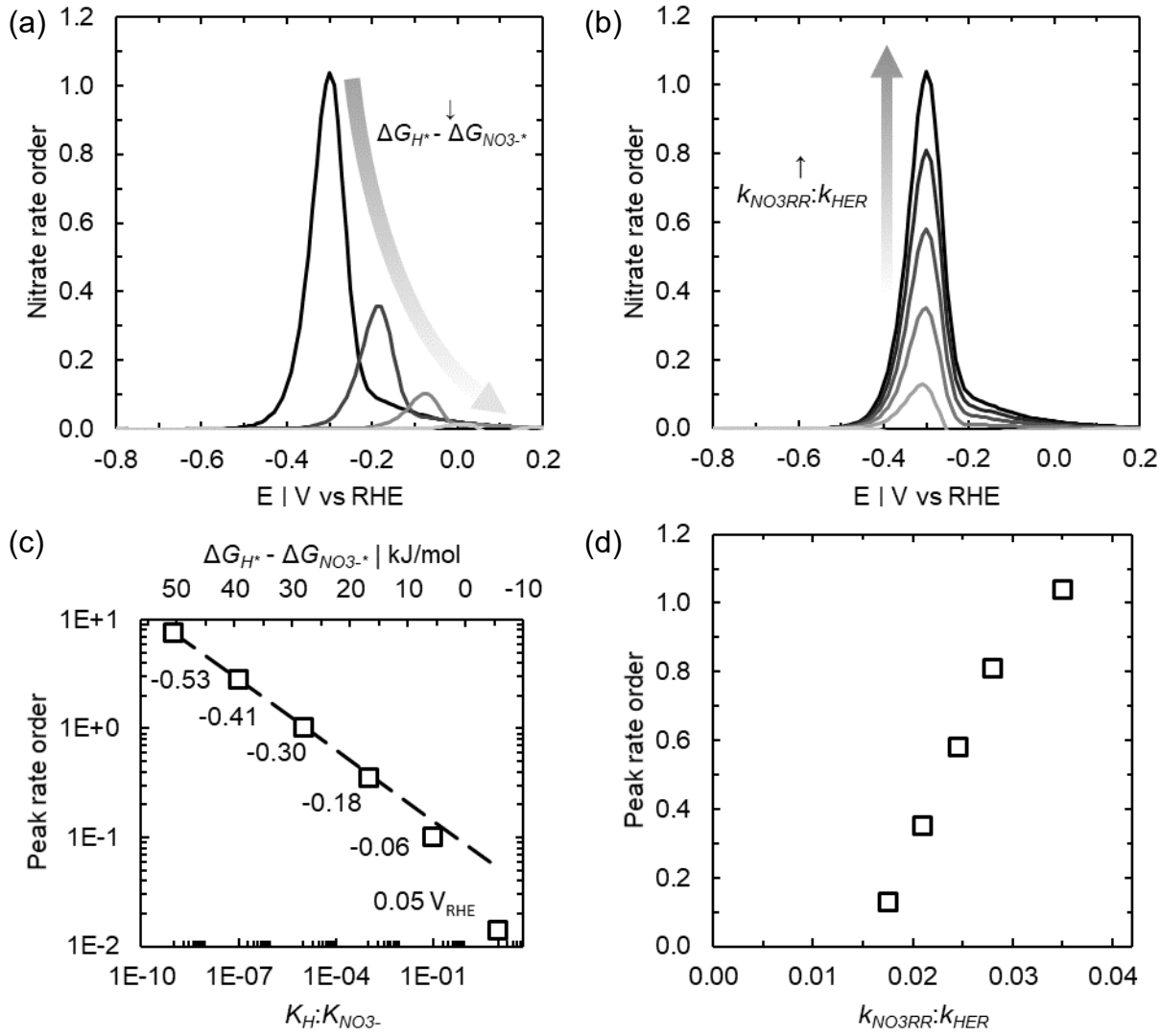

Supplementary Figure 13. (a) Nitrate rate order for a series of H^* to nitrate adsorption coefficients ($K_H/K_{NO_3^-}$) denoted by increasingly light shades in order of 10^{-5}, 10^{-3}, 10^{-1}, and 10^{1}. Kinetic parameters used are the same as in Supplementary Figure 12, but with $k_{5F}^0 = k_{6F}^0 = k_{7F}^0 = 10^{-9}$. (b) Nitrate rate order at a fixed $K_H/K_{NO_3^-}$ of 10^{-5} for a series of HER and NO_3RR reaction rate constant ratios ($k_{1F}^0 = k_{2F}^0 = k_{3F}^0 = 1.0\text{x}10^{-9}$ and $k_{5F}^0 = k_{6F}^0 = k_{7F}^0 = 3.5\text{x}10^{-11}$, $7.0\text{x}10^{-12}$, $2.8\text{x}10^{-11}$, $2.5\text{x}10^{-11}$, $2.1\text{x}10^{-11}$, and $1.8\text{x}10^{-11}$ in increasingly dark shades of black). Peak nitrate rate order vs (c) $K_H/K_{NO_3^-}$ and ΔG_{H^*} - ΔG_{NO3-*} with peak potential denoted vs RHE, or (d) k_{NO3RR}:k_{HER}. The line in (c) is a linear regression of the points with the highest three rate orders ($K_H/K_{NO_3^-}$ of 10^{-9}, 10^{-7},and 10^{-5}).

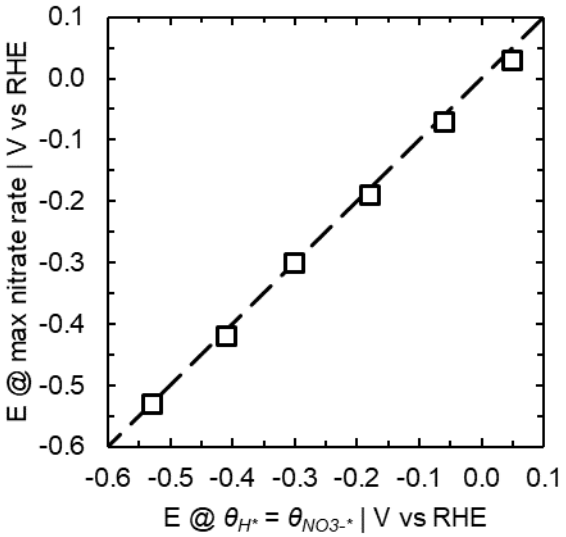

Supplementary Figure 14. Parity plot of potential at maximum nitrate rate against the potential at which H^* coverage exceeds that of nitrate, illustrating the dependence of maximum nitrate rate on nitrate and H^* coverage.

While thermodynamic parameters (ratio of H^* to nitrate adsorption coefficients $[K_H/K_{NO_3^-}]$ or difference in free energy of adsorption $[\Delta G_{H*} - \Delta G_{NO_3^-*}]$) dictate the potential and magnitude of peak nitrate rate order (Supplementary Figure 13a,c), kinetic parameters (ratios of reaction rate constants [k_{NO3RR}:k_{HER}]) dictate only magnitude (Supplementary Figure 13b,d). As k_{NO3RR}:k_{HER} is increased, peak rate order increases while the potential remains constant. Even when incorporating material- and potential-dependent n_{NO_3RR} (Figures S16 and S17 and Supplementary Table 2) the message from the main text is preserved; nitrate rate order peak potential and magnitude are predominantly controlled by $\Delta G_{H*} - \Delta G_{NO_3^-*}$ (Supplementary Figure 15a), with only minor manipulations of kinetic parameters (Supplementary Table 1) required to fully capture peak rate order and potential (Supplementary Figure 15b).

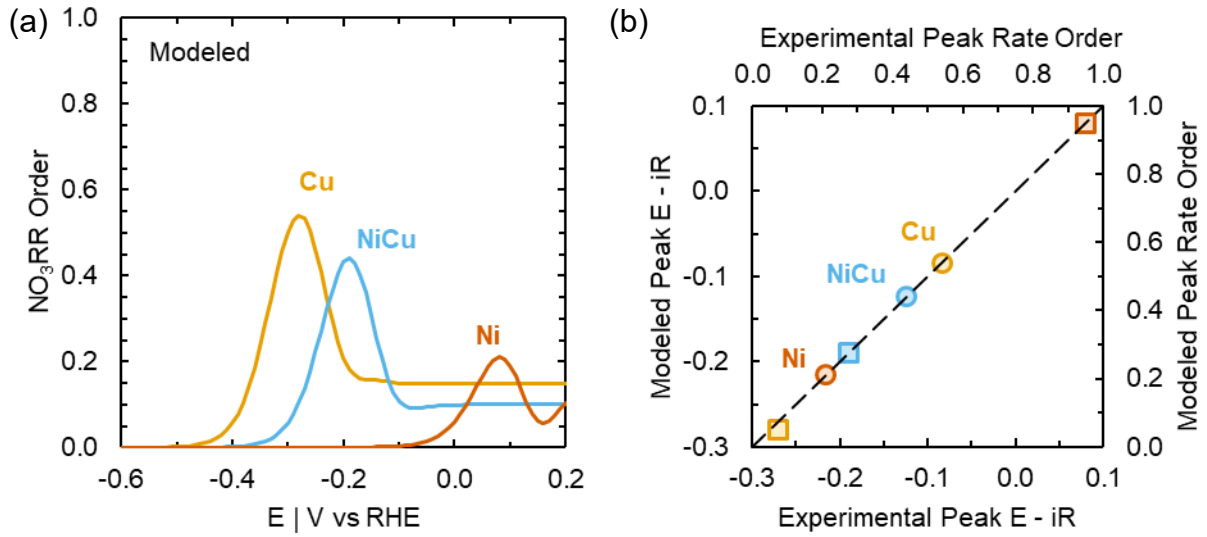

Supplementary Figure 15. (a) Modeled nitrate rate order data, inclusive of experimental selectivity data: model parameters provided in Supplementary Table 1. (b) Parity plot of experimental (x-axes) and modeled (y-axes) potential (primary axes, squares) and magnitude of peak nitrate rate order (secondary axes, circles) for Cu (golden), $Ni_{0.68}Cu_{0.32}$ (blue), and Ni (orange) as denoted.

Supplementary Table 1. Parameters used to produce microkinetic model results in Supplementary Figure 15 and Figure 2.

		Supplementary Figure 15			**Figure 2**		
	Metals	Cu	$Ni_{0.68}Cu_{0.32}$	Ni	Cu	$Ni_{0.68}Cu_{0.32}$	Ni
Conc. and Selectivity	α_{H^+} | M	0.1	0.1	0.1	0.1	0.1	0.1
	$\alpha_{NO_3^-}$ | M	0.1	0.1	0.1	0.1	0.1	0.1
	n_{HER}	2	2	2	2	2	2
	n_{NO_3RR}	f(E)	f(E)	f(E)	2	2	2
Thermo	K_H	$3.0x10^{-3}$	$9.0x10^{-2}$	$4.0x10^{3}$	$3.5x10^{-3}$	$1.0x10^{-1}$	$5.0x10^{3}$
	ΔG_{H*} | kJ/mol	14.2	5.9	-20.2	13.8	5.6	-20.8
	$K_{NO_3^-}$	$1.0x10^{2}$	$1.0x10^{2}$	$1.0x10^{2}$	$1.0x10^{2}$	$1.0x10^{2}$	$1.0x10^{2}$
	$\Delta G_{NO_3^-*}$ | kJ/mol	-11.2	-11.2	-11.2	-11.2	-11.2	-11.2
	$K_H/K_{NO_3^-}$	$3.0x10^{-5}$	$9.0x10^{-4}$	$4.0x10^{1}$	$3.5x10^{-5}$	$1.0x10^{-3}$	$5.0x10^{1}$
	$\boldsymbol{\Delta G_{H*} - \Delta G_{NO_3^-*}}$	25.4	17.1	-9.0	25.0	16.8	-9.5
Kinetics	η_{HER} | VRHE	0	0	0	0	0	0
	η_{NO_3RR} | VRHE	0.82	0.82	0.82	0.82	0.82	0.82
	α	0.21	0.21	0.21	0.21	0.21	0.21
	k_{1F}^0 | L/s-cm^2	$5.0x10^{-10}$	$5.0x10^{-10}$	$5.0x10^{-10}$	$5.0x10^{-10}$	$5.0x10^{-10}$	$5.0x10^{-10}$
	k_{2F}^0 | L/s-cm^2	$1.0x10^{-10}$	$1.0x10^{-10}$	$1.0x10^{-10}$	$5.0x10^{-11}$	$5.0x10^{-11}$	$5.0x10^{-11}$
	k_{3F}^0 | mol/s-cm^2	$1.0x10^{-10}$	$1.0x10^{-10}$	$1.0x10^{-10}$	$5.0x10^{-11}$	$5.0x10^{-11}$	$5.0x10^{-11}$
	k_{5F}^0 | L^2/mol-s-cm^2	$9.3x10^{-12}$	$3.3x10^{-12}$	$3.3x10^{-12}$	$1.0x10^{-11}$	$1.0x10^{-11}$	$1.0x10^{-11}$
	k_{6F}^0 | mol/s-cm^2	$6.1x10^{-12}$	$2.8x10^{-12}$	$4.2x10^{-12}$	$2.5x10^{-12}$	$2.5x10^{-12}$	$2.5x10^{-12}$
	k_{7F}^0 | L/s-cm^2	$6.1x10^{-12}$	$2.8x10^{-12}$	$4.2x10^{-12}$	$5.0x10^{-10}$	$5.0x10^{-10}$	$5.0x10^{-10}$

2.3. Selectivity

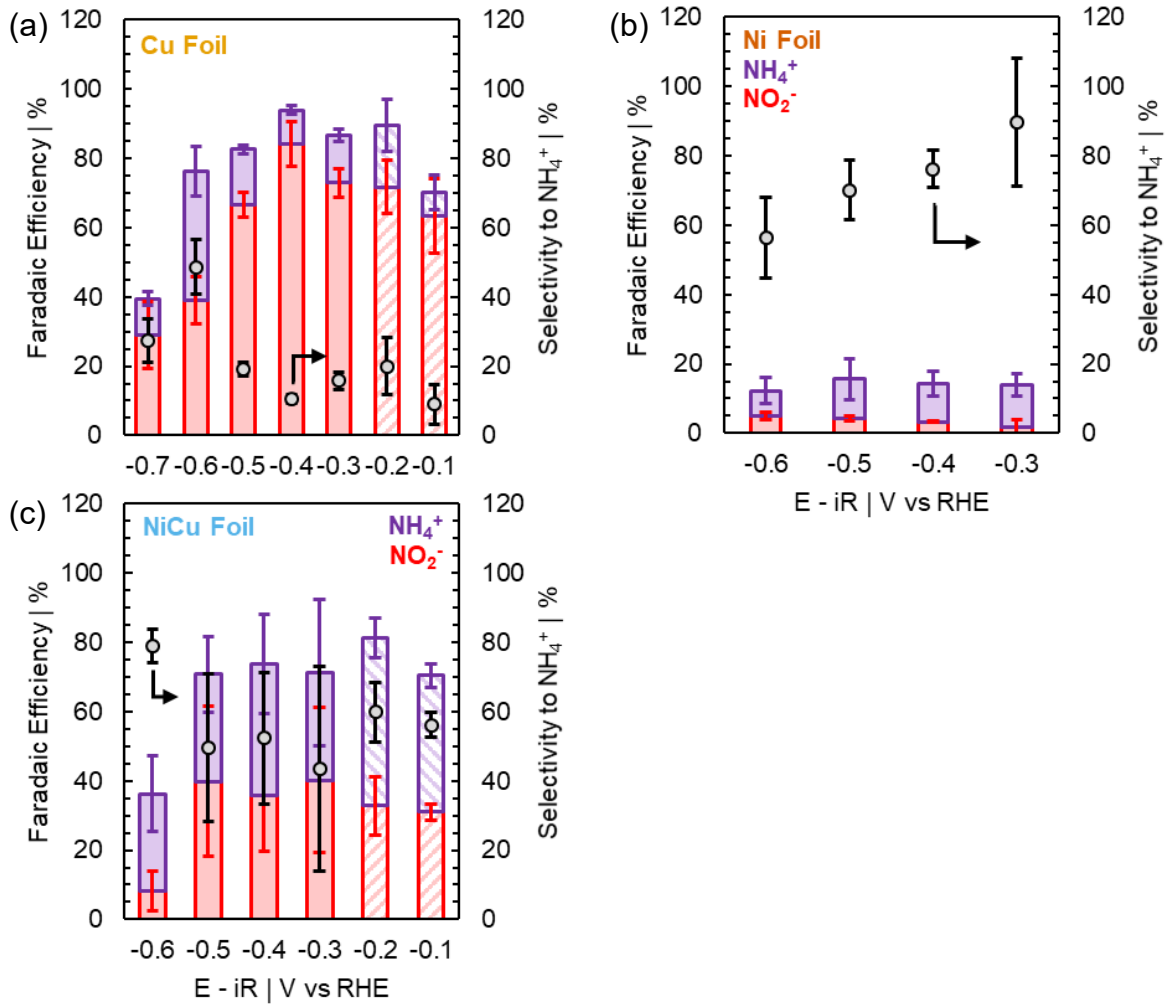

Supplementary Figure 16. FE to nitrite (red bars) and ammonium (purple bars) after passing 0.2 e^-/NO_3^- (solid) or 0.04 e^-/NO_3^- (hatched) by 85% iR-corrected CA for (a) Cu, (b) Ni, and (c) $Ni_{0.68}Cu_{0.32}$ foils. Selectivity to ammonium reported as circular symbols. Selectivity data for each metal are provided in a potential-resolved tabulated format as Supplementary Table 2. Error bars denote plus and minus one standard deviation of the average of at least three (n = 3) separate measurements.

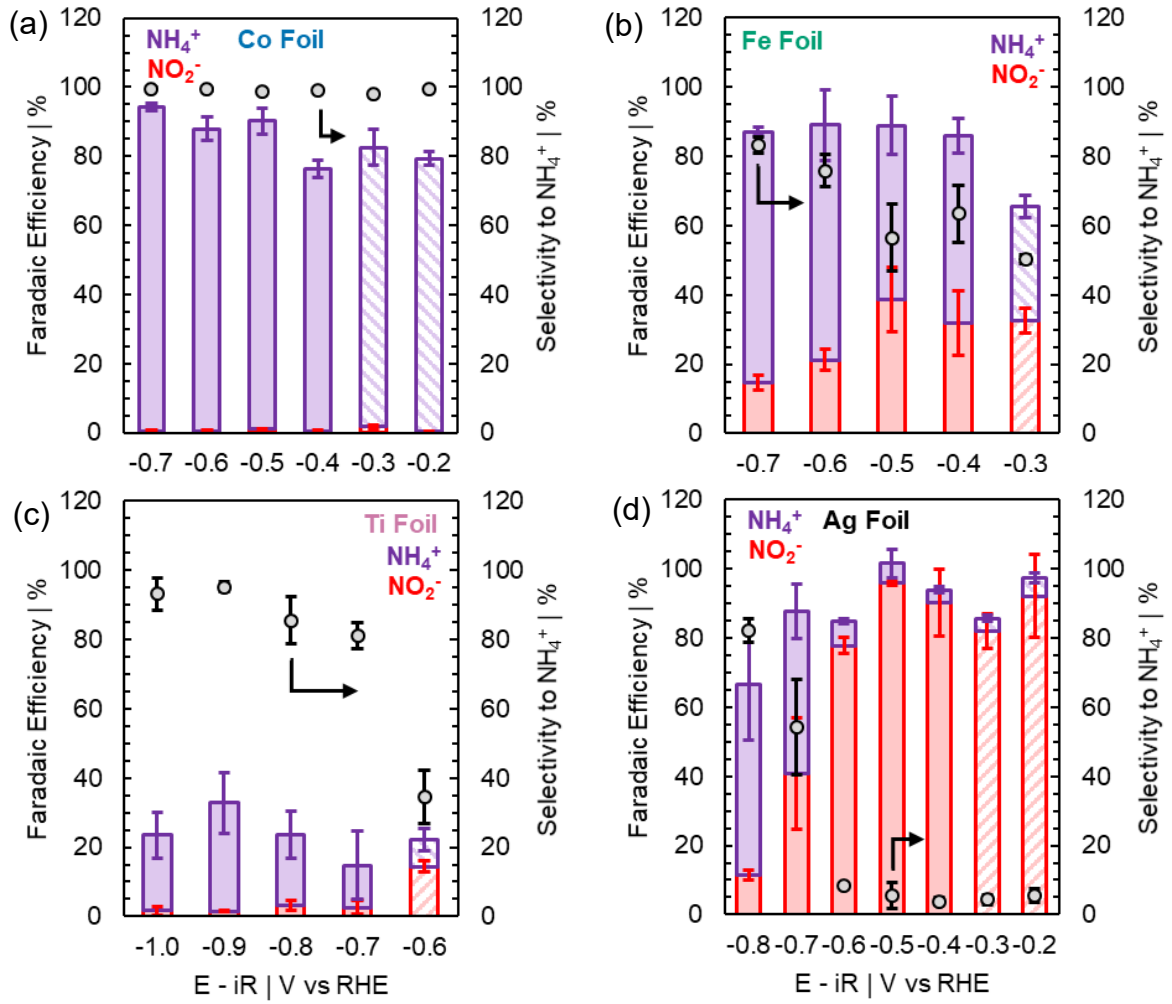

Supplementary Figure 17. FE to nitrite (red bars) and ammonium (purple bars) after passing 0.2 e^-/NO_3^- (solid) or 0.04 e^-/NO_3^- (hatched) by 85% iR-corrected CA for (a) Co, (b) Fe, (c) Ti, and (d) Ag foils. Selectivity to ammonium reported as circular symbols. Selectivity data for each metal are provided in a potential-resolved tabulated format as Supplementary Table 2. Error bars denote plus and minus one standard deviation of the average of at least three (n = 3) separate measurements.

Supplementary Table 2. Average of potential-resolved FE to nitrite and ammonium for each TM foil, plus and minus one standard deviation from the average of at least three (n = 3) samples. Dashes denote no measurement made.

E - iR | V_{RHE}		-0.1	-0.2	-0.3	-0.4	-0.5	-0.6	-0.7	-0.8	-0.9	-1.0
FE to NO_2^- | %	Cu	63.5 ± 10.7	71.7 ± 7.7	72.9 ± 4.0	84.1 ± 6.5	66.7 ± 3.6	39.1 ± 6.8	28.9 ± 9.7	- - -	- - -	- - -
	Ni	- - -	- - -	1.6 ± 2.4	3.3 ± 0.2	4.3 ± 0.6	5.0 ± 1.0	- - -	- - -	- - -	- - -
	NiCu	31.0 ± 2.4	32.9 ± 8.5	40.2 ± 21.0	35.8 ± 16.3	39.9 ± 21.8	8.2 ± 5.7	- - -	- - -	- - -	- - -
	Co	- - -	- - -	1.7 ± 0.5	0.6 ± 0.2	1.0 ± 0.3	0.5 ± 0.3	0.5 ± 0.3	- - -	- - -	- - -
	Fe	- - -	- - -	32.5 ± 3.7	31.9 ± 9.4	38.8 ± 9.3	21.3 ± 3.1	14.7 ± 2.3	- - -	- - -	- - -
	Ti	- - -	- - -	- - -	- - -	- - -	- - -	2.6 ± 2.0	3.3 ± 1.5	1.5 ± 0.3	1.6 ± 1.1
	Ag	- - -	92.1 ± 12.0	82.1 ± 5.0	90.3 ± 9.6	95.8 ± 0.6	77.8 ± 2.3	40.8 ± 16.0	11.4 ± 1.4	- - -	- - -
FE to NH_4^+ | %	Cu	6.6 ± 5.0	17.8 ± 7.5	13.6 ± 1.8	9.9 ± 1.3	15.8 ± 1.2	37.2 ± 7.1	10.5 ± 2.0	- - -	- - -	- - -
	Ni	- - -	- - -	12.3 ± 3.1	11.0 ± 3.5	11.3 ± 5.9	7.3 ± 3.8	- - -	- - -	- - -	- - -
	NiCu	39.4 ± 3.2	48.5 ± 5.8	31.0 ± 21.0	38.1 ± 0.0	30.9 ± 10.9	28.1 ± 10.8	- - -	- - -	- - -	- - -
	Co	- - -	- - -	80.9 ± 5.2	75.8 ± 2.5	89.2 ± 3.7	87.4 ± 3.4	93.7 ± 1.0	- - -	- - -	- - -
	Fe	- - -	- - -	32.9 ± 3.2	54.1 ± 5.0	50.2 ± 8.3	67.7 ± 10.2	72.5 ± 1.2	- - -	- - -	- - -
	Ti	- - -	- - -	- - -	- - -	- - -	- - -	12.2 ± 9.8	20.3 ± 6.8	31.4 ± 8.8	21.9 ± 6.6
	Ag	- - -	5.4 ± 1.5	3.7 ± 1.1	3.6 ± 0.8	5.7 ± 4.1	7.2 ± 0.7	46.9 ± 7.8	55.1 ± 16.0	- - -	- - -

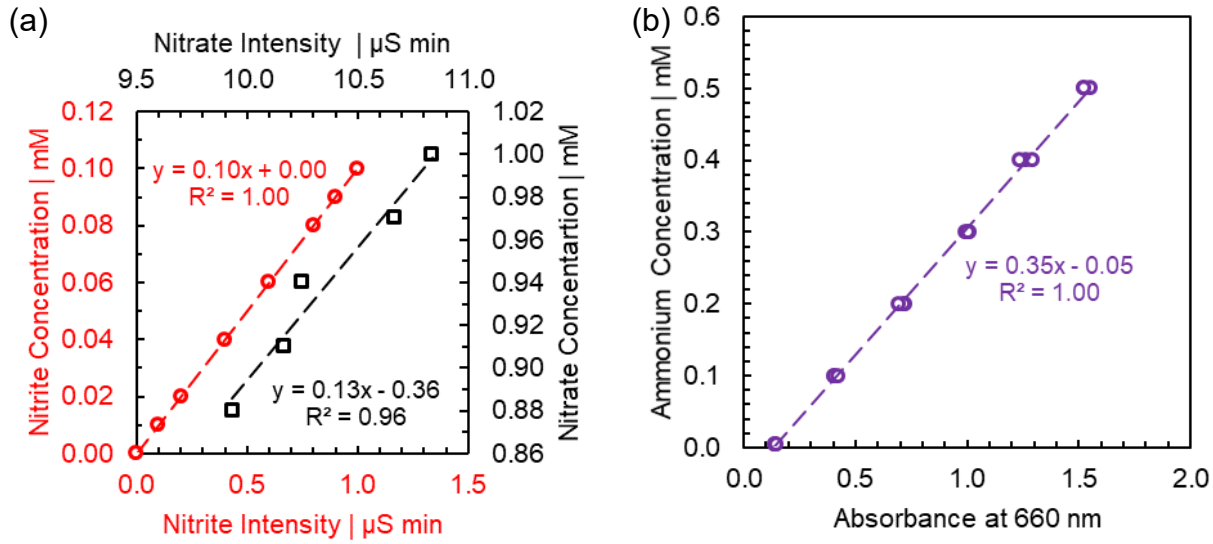

Supplementary Figure 18. Typical examples of calibration curves for (a) nitrite and nitrate by anion IC and (b) ammonium by spectrophotometric plate reading. Note, calibration curves and samples for (a) anion IC are diluted by 100x and (b) 5x for spectrophotometry.

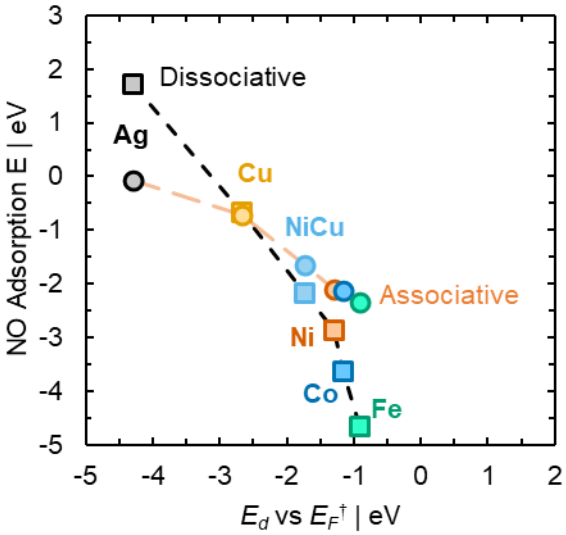

Supplementary Figure 19. Calculated nitric oxide adsorption energy against E_d vs E_F for the series of stepped TM surfaces investigated here, illustrating the dependence of adsorbate binding energies on critical electronic structure descriptors such as E_d vs E_F. † Data for E_d vs E_F adapted from Ref. [51] and NO adsorption energies from Ref. [52].

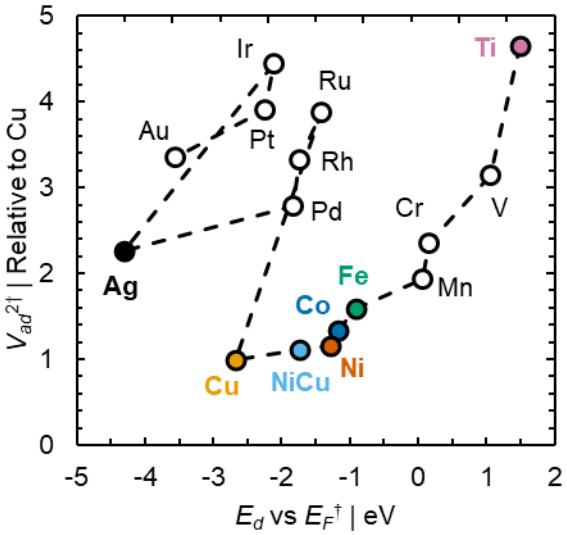

Supplementary Figure 20. Pauli repulsion term against E_d vs E_F for select 3rd, 4th, and 5th row TMs. † Data for E_d vs E_F and V_{ad}^2 adapted from Ref. [51].

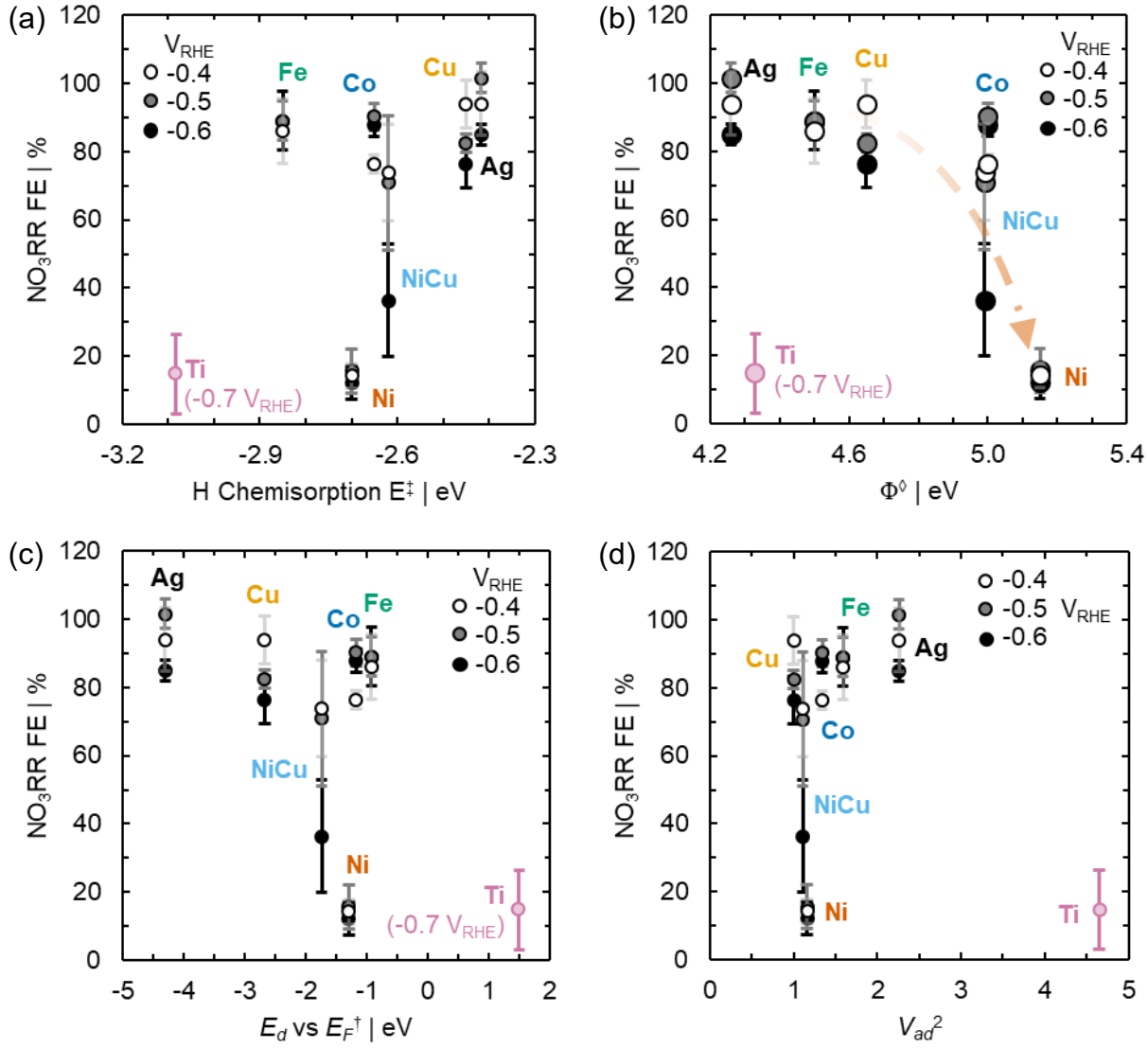

Supplementary Figure 21. NO_3RR FE against (a) H chemisorption energy, (b) work function, (c) E_d vs E_F, and (d) V_{ad}^2 for a series of TM foils and measured by 85% iR-corrected CA to 0.2 e^-/NO_3^-. ‡ ◊ † Data for H chemisorption energy adapted from Ref. [28], work function from Ref. [27], and E_d vs E_F and V_{ad}^2 from Ref. [51].

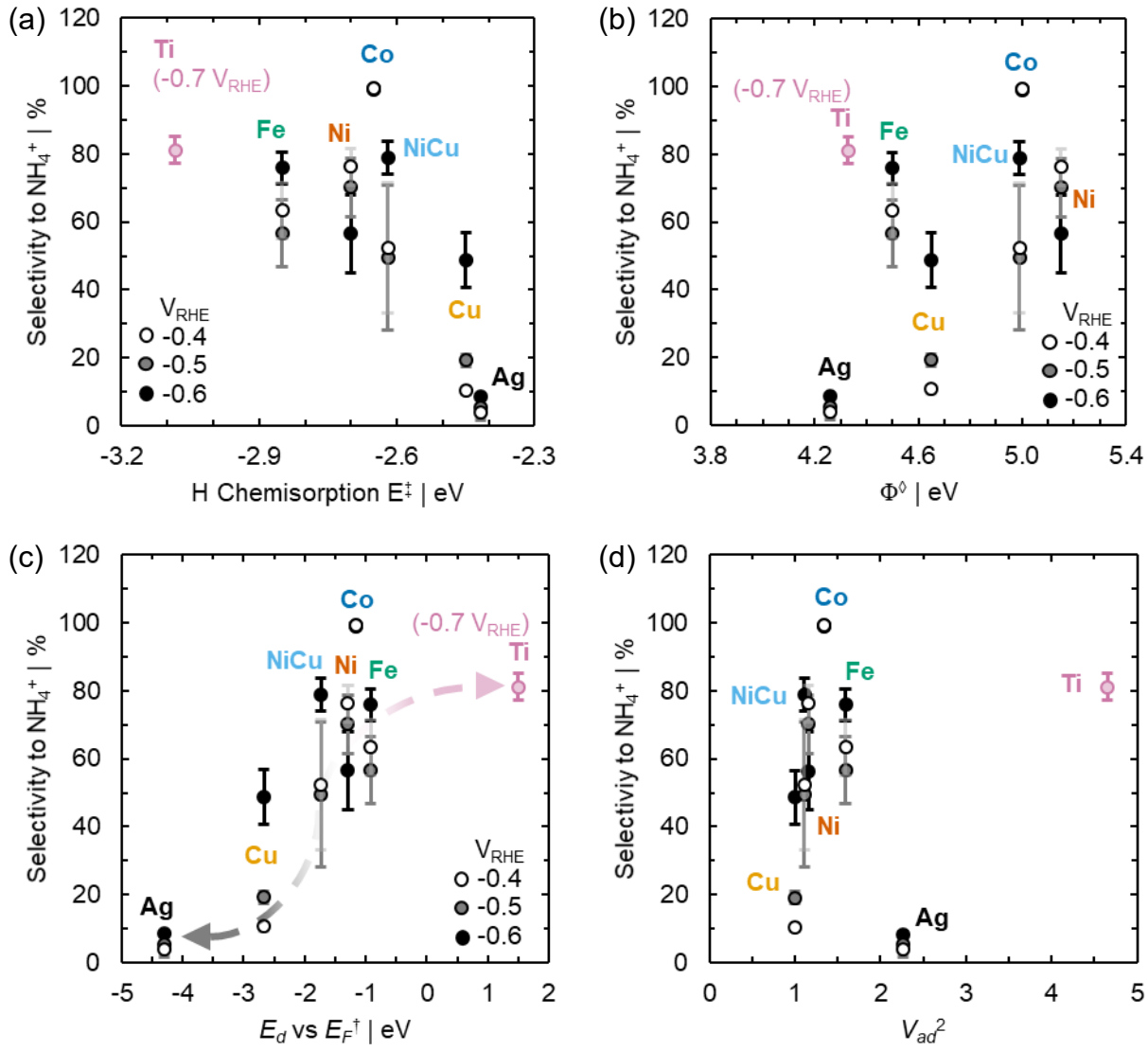

Supplementary Figure 22. Selectivity towards ammonium against (a) H chemisorption energy, (b) work function, (c) E_d vs E_F, and (d) V_{ad}^2 for a series of TM foils and measured by 85% iR-corrected CA to 0.2 e^-/NO_3^-. ‡ ◊ † Data for H chemisorption energy adapted from Ref. [28], work function from Ref. [27], and E_d vs E_F and V_{ad}^2 from Ref. [51].

2.4. Density functional theory figures

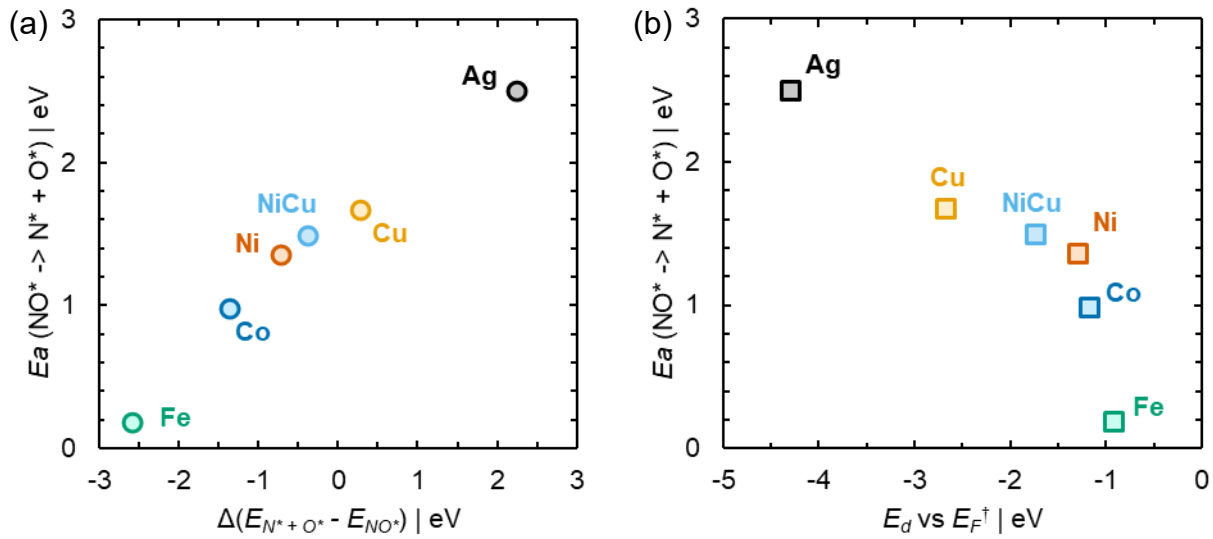

Supplementary Figure 23. (a) The activation barrier (*Ea*) for dissociation of adsorbed nitric oxide (NO^*) into nitrogen and oxygen adatoms (N^* + O^*) decreases in concert with the enthalpy of dissociation ($\Delta(E_{N*+O*} - E_{NO*})$), in-line with Bronsted-Evans-Polanyi scaling relationships. (b) Activation barrier for dissociation of adsorbed nitric oxide against E_d vs E_F. † Values for E_d vs E_F from Ref. [51].

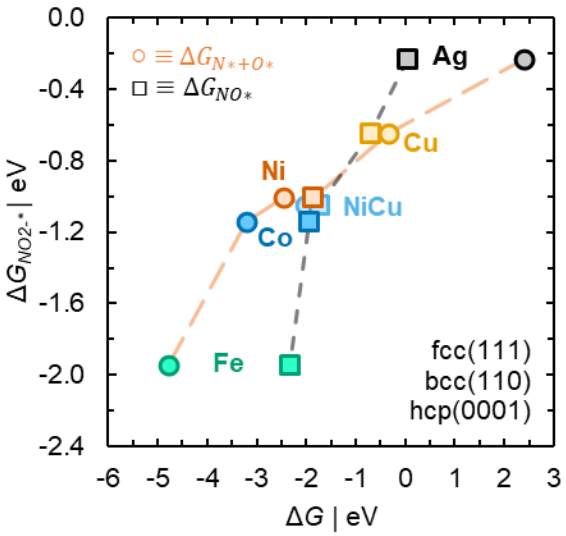

Supplementary Figure 24. Nitrite free energy of adsorption against that of associative (circles with long orange lines) or dissociative (squares with short black lines) nitric oxide adsorption for a series of denoted TM foils. $NO_{(g)}$ was used as a reference state for ΔG_{NO*} and ΔG_{N*+O*} calculations, while $NO_{2\,(g)}$ was used as reference state for $\Delta G_{NO_2^-*}$ calculations.

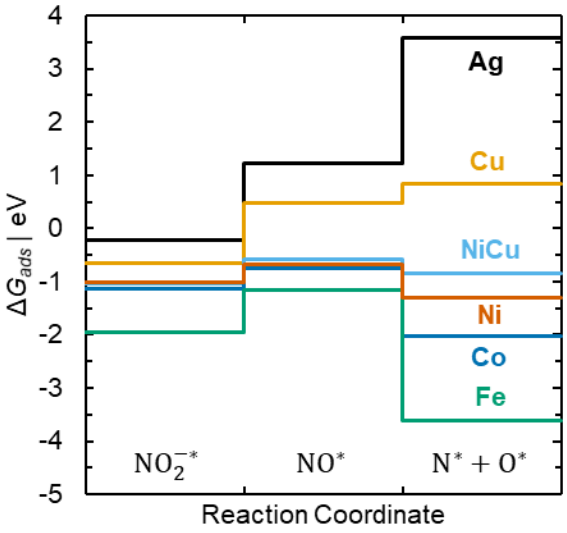

Supplementary Figure 25. Calculated free energy of reaction coordinate for the reduction of adsorbed nitrite (NO_2^{-*}) to nitric oxide (NO^*), and its subsequent dissociation ($N^* + O^*$) for the denoted TMs. $NO_{2(g)}$ used as reference state with ½ $O_{2(g)}$ included for ΔG_{NO*} and ΔG_{N*+O*}.

Supplementary Table 3. Adsorption enthalpies (ΔE_{ads}) and free energies (ΔG_{ads}) for nitrite and molecular and dissociated nitric oxide on a series of low-energy TM surfaces.

	Element	Ti	Fe	Co	Ni	$Ni_{0.67}Cu_{0.33}$	Cu	Ag
	Phase	hcp	bcc	hcp	fcc	fcc	fcc	fcc
	Orientation	(0001)	(110)	(0001)	(111)	(111)	(111)	(111)
$NO_{(g)}$ ref. eV	ΔE_{NO}	-5.46	-2.81	-2.46	-2.39	-2.26	-1.21	-0.40
	ΔE_{N+O}	-5.46	-5.39	-3.83	-3.12	-2.65	-0.94	1.84
	ΔG_{NO}	-4.90	-2.32	-1.94	-1.86	-1.74	-0.70	0.06
	ΔG_{N+O}	-4.90	-4.78	-3.20	-2.47	-2.02	-0.34	2.40
$NO_{2(g)}$ ref. eV	$\Delta E_{NO_2^-}$	-10.11	-2.51	-1.67	-1.55	-1.60	-1.17	-0.64
	ΔE_{NO}	-4.29	-1.63	-1.29	-1.22	-1.08	-0.03	0.77
	ΔE_{N+O}	-4.29	-4.21	-2.66	-1.94	-1.47	0.24	3.01
	$\Delta G_{NO_2^-}$	-9.49	-1.94	-1.14	-1.00	-1.05	-0.65	-0.23
	ΔG_{NO}	-3.73	-1.15	-0.76	-0.68	-0.57	0.48	1.23
	ΔG_{N+O}	-3.73	-3.61	-2.02	-1.29	-0.84	0.84	3.57

3. References

1. Liu, M. J. *et al.* Catalytic Performance and Near-Surface X-ray Characterization of Titanium Hydride Electrodes for the Electrochemical Nitrate Reduction Reaction. *J. Am. Chem. Soc.* **144**, 5739–5744 (2022).
2. Pourbaix, M. *Atlas of electrochemical equilibria in aqueous solutions*. (National Association of Corrosion Engineers, 1966).
3. Wei, C. *et al.* Recommended Practices and Benchmark Activity for Hydrogen and Oxygen Electrocatalysis in Water Splitting and Fuel Cells. *Adv. Mater.* **31**, 1806296 (2019).
4. van der Vliet, D. *et al.* On the importance of correcting for the uncompensated Ohmic resistance in model experiments of the Oxygen Reduction Reaction. *J. Electroanal. Chem.* **647**, 29–34 (2010).
5. Morales, D. M. & Risch, M. Seven steps to reliable cyclic voltammetry measurements for the determination of double layer capacitance. *J. Phys. Energy* (2021).
6. Carvalho, O. Q. *et al.* Role of oxide support in electrocatalytic nitrate reduction on Cu. *Electrochem. Sci. Adv.* Under Review (2022).
7. Rhine, E. D., Mulvaney, R. L., Pratt, E. J. & Sims, G. K. Improving the Berthelot Reaction for Determining Ammonium in Soil Extracts and Water. *Soil Sci. Soc. Am. J.* **62**, 473–480 (1998).
8. Kresse, G. & Hafner, J. Ab initio molecular dynamics for liquid metals. *Phys. Rev. B* **47**, 558–561 (1993).
9. Kresse, G. & Furthmüller, J. Efficiency of ab-initio total energy calculations for metals and semiconductors using a plane-wave basis set. *Comput. Mater. Sci.* **6**, 15–50 (1996).
10. Kresse, G. & Hafner, J. Ab initio molecular-dynamics simulation of the liquid-metal--amorphous-semiconductor transition in germanium. *Phys. Rev. B* **49**, 14251–14269 (1994).
11. Perdew, J. P., Burke, K. & Ernzerhof, M. Generalized Gradient Approximation Made Simple [Phys. Rev. Lett. 77, 3865 (1996)]. *Phys. Rev. Lett.* **78**, 1396 (1997).
12. Blöchl, P. E. Projector augmented-wave method. *Phys. Rev. B* **50**, 17953–17979 (1994).
13. Kresse, G. & Joubert, D. From ultrasoft pseudopotentials to the projector augmented-wave method. *Phys. Rev. B* **59**, 1758–1775 (1999).
14. Davey, W. P. Precision Measurements of the Lattice Constants of Twelve Common Metals. *Phys. Rev.* **25**, 753–761 (1925).
15. Wood, R. M. The Lattice Constants of High Purity Alpha Titanium. *Proc. Phys. Soc.* **80**, 783–786 (1962).
16. Ono, F. & Maeta, H. DETERMINATION OF LATTICE PARAMETERS IN HCP COBALT BY USING X-RAY BOND'S METHOD. *http://dx.doi.org/10.1051/jphyscol:1988818* **49**, (1988).
17. Best, R. J. & Russell, W. W. Nickel, Copper and Some of their Alloys as Catalysts for Ethylene Hydrogenation1. *J. Am. Chem. Soc.* **76**, 838–842 (1954).
18. Patra, A., Jana, S., Constantin, L. A., Chiodo, L. & Samal, P. Improved transition metal surface energies from a generalized gradient approximation developed for quasi two-dimensional systems. *J. Chem. Phys.* **152**, 151101 (2020).
19. Methfessel, M. & Paxton, A. T. High-precision sampling for Brillouin-zone integration in metals. *Phys. Rev. B* **40**, 3616–3621 (1989).
20. Henkelman, G. & Jónsson, H. Improved tangent estimate in the nudged elastic band method for finding

minimum energy paths and saddle points. *J. Chem. Phys.* **113**, 9978–9985 (2000).
21. Henkelman, G., Uberuaga, B. P. & Jónsson, H. A climbing image nudged elastic band method for finding saddle points and minimum energy paths. *J. Chem. Phys.* **113**, 9901–9904 (2000).
22. Sheppard, D., Terrell, R. & Henkelman, G. Optimization methods for finding minimum energy paths. *J. Chem. Phys.* **128**, 134106 (2008).
23. Hall, D. S., Bock, C. & MacDougall, B. R. The Electrochemistry of Metallic Nickel: Oxides, Hydroxides, Hydrides and Alkaline Hydrogen Evolution. *J. Electrochem. Soc.* **160**, F235–F243 (2013).
24. Oshchepkov, A. G., Braesch, G., Bonnefont, A., Savinova, E. R. & Chatenet, M. Recent Advances in the Understanding of Nickel-Based Catalysts for the Oxidation of Hydrogen-Containing Fuels in Alkaline Media. *ACS Catal.* **10**, 7043–7068 (2020).
25. Obata, K., Stegenburga, L. & Takanabe, K. Maximizing Hydrogen Evolution Performance on Pt in Buffered Solutions: Mass Transfer Constrains of H2 and Buffer Ions. *J. Phys. Chem. C* **123**, 21554–21563 (2019).
26. Vos, J. G. & Koper, M. T. M. Examination and prevention of ring collection failure during gas-evolving reactions on a rotating ring-disk electrode. *J. Electroanal. Chem.* **850**, 113363 (2019).
27. Michaelson, H. B. The work function of the elements and its periodicity. *J. Appl. Phys.* **48**, 4729–4733 (1977).
28. Nordlander, P., Holloway, S. & Nørskov, J. K. Hydrogen adsorption on metal surfaces. *Surf. Sci.* **136**, 59–81 (1984).
29. Wang, Z., Richards, D. & Singh, N. Recent discoveries in the reaction mechanism of heterogeneous electrocatalytic nitrate reduction. *Catal. Sci. Technol.* **11**, 705–725 (2021).
30. Dima, G. E., De Vooys, A. C. A. & Koper, M. T. M. Electrocatalytic reduction of nitrate at low concentration on coinage and transition-metal electrodes in acid solutions. *J. Electroanal. Chem.* **554–555**, 15–23 (2003).
31. Rosca, V., Duca, M., de Groot, M. T. & Koper, M. T. M. Nitrogen Cycle Electrocatalysis. *Chem. Rev.* **109**, 2209–2244 (2009).
32. Badea, G. E. Electrocatalytic reduction of nitrate on copper electrode in alkaline solution. *Electrochim. Acta* **54**, 996–1001 (2009).
33. Bouzek, K., Paidar, M., Sadílková, A. & Bergmann, H. Electrochemical reduction of nitrate in weakly alkaline solutions. *J. Appl. Electrochem.* **31**, 1185–1193 (2001).
34. Shih, Y.-J., Wu, Z.-L., Huang, Y.-H. & Huang, C.-P. Electrochemical nitrate reduction as affected by the crystal morphology and facet of copper nanoparticles supported on nickel foam electrodes (Cu/Ni). *Chem. Eng. J.* **383**, 123157 (2020).
35. Wang, Y. *et al.* Enhanced Nitrate-to-Ammonia Activity on Copper–Nickel Alloys via Tuning of Intermediate Adsorption. *J. Am. Chem. Soc.* **142**, 5702–5708 (2020).
36. Wei, C. *et al.* Surface Composition Dependent Ligand Effect in Tuning the Activity of Nickel–Copper Bimetallic Electrocatalysts toward Hydrogen Evolution in Alkaline. *J. Am. Chem. Soc.* **142**, 7765–7775 (2020).
37. Singh, N. *et al.* Quantifying Adsorption of Organic Molecules on Platinum in Aqueous Phase by Hydrogen Site Blocking and in Situ X-ray Absorption Spectroscopy. *ACS Catal.* **9**, 6869–6881 (2019).
38. Singh, N. *et al.* Aqueous phase catalytic and electrocatalytic hydrogenation of phenol and benzaldehyde over platinum group metals. *J. Catal.* (2020) doi:10.1016/j.jcat.2019.12.034.

39. Akinola, J., Campbell, C. T. & Singh, N. Effects of Solvents on Adsorption Energies: A General Bond-Additivity Model. *J. Phys. Chem. C* **125**, 24371–24380 (2021).
40. Shinagawa, T., Garcia-Esparza, A. T. & Takanabe, K. Insight on Tafel slopes from a microkinetic analysis of aqueous electrocatalysis for energy conversion. *Sci. Rep.* **5**, 13801 (2015).
41. Dima, G. E., Beltramo, G. L. & Koper, M. T. M. Nitrate reduction on single-crystal platinum electrodes. *Electrochim. Acta* **50**, 4318–4326 (2005).
42. Huang, H., Zhao, M., Xing, X., Bae, I. T. & Scherson, D. In-situ infrared studies of the Cd-UPD mediated reduction of nitrate on gold. *J. Electroanal. Chem. Interfacial Electrochem.* **293**, 279–284 (1990).
43. De, D., Kalu, E. E., Tarjan, P. P. & Englehardt, J. D. Kinetic Studies of the Electrochemical Treatment of Nitrate and Nitrite Ions on Iridium-Modified Carbon Fiber Electrodes. *Chem. Eng. Technol.* **27**, 56–64 (2004).
44. Shimazu, K. *et al.* Reduction of nitrate ions on tin-modified palladium thin film electrodes. *J. Electroanal. Chem.* **601**, 161–168 (2007).
45. Tada, K. & Shimazu, K. Kinetic studies of reduction of nitrate ions at Sn-modified Pt electrodes using a quartz crystal microbalance. *J. Electroanal. Chem.* **577**, 303–309 (2005).
46. Liu, J.-X., Richards, D., Singh, N. & Goldsmith, B. R. Activity and Selectivity Trends in Electrocatalytic Nitrate Reduction on Transition Metals. *ACS Catal.* **9**, 7052–7064 (2019).
47. Vanysek, P. *CRC Handbook of Chemistry and Physics*. (CRC Press, 2011).
48. Nesbitt, N. T. & Smith, W. A. Water and Solute Activities Regulate CO2 Reduction in Gas-Diffusion Electrodes. *J. Phys. Chem. C* **125**, 13085–13095 (2021).
49. Bratsch, S. G. Standard Electrode Potentials and Temperature Coefficients in Water at 298.15 K. *J. Phys. Chem. Ref. Data* **18**, 1–21 (1989).
50. Bard, A. J. & Faulkner, L. R. *Electrochemical Methods: Fundamentals and Applications*. (John Wiley & Sons, Ltd, 2001).
51. Hammer, B. & Nørskov, J. K. Theoretical surface science and catalysis—calculations and concepts. *Adv. Catal.* **45**, 71–129 (2000).
52. Bligaard, T. *et al.* The Brønsted–Evans–Polanyi relation and the volcano curve in heterogeneous catalysis. *J. Catal.* **224**, 206–217 (2004).